

Shocks in the symbiotic recurrent nova V3890 Sgr: VLBI radio imaging and Fermi GeV gamma-rays

Downloaded from: https://research.chalmers.se, 2026-11-07 23:06 UTC

Citation for the original published paper (version of record):

Molina, I., Craig, P., Diesing, R. et al (2026). Shocks in the symbiotic recurrent nova V3890 Sgr: VLBI radio imaging and Fermi GeV gamma-rays. Monthly Notices of the Royal Astronomical Society, 552(4). http://dx.doi.org/10.1093/mnras/stag1851

N.B. When citing this work, cite the original published paper.

research.chalmers.se offers the possibility of retrieving research publications produced at Chalmers University of Technology. It covers all kind of research output: articles, dissertations, conference papers, reports etc. since 2004. research.chalmers.se is administrated and maintained by Chalmers Library

(article starts on next page)

Monthly Notices of the ROYAL ASTRONOMICAL SOCIETY

MNRAS **552,** 1–19 (2026)
Advance Access publication 2026 September 28

https://doi.org/10.1093/mnras/stag1851

Shocks in the symbiotic recurrent nova V3890 Sgr: VLBI radio imaging and *Fermi* GeV gamma-rays

Isabella Molina [1]★, Peter Craig [1], Rebecca Diesing[2,3], Laura Chomiuk[1], Justin D. Linford [4], Brian D. Metzger[3,5], Jun Yang [6], Brandon Benavente[1], Kim L. Page [7], Kirill V. Sokolovsky [8], Elias Aydi [9], Amy J. Mioduszewski[4], Koji Mukai [10,11], Miriam M. Nyamai[12], Michael P. Rupen[13], J. L. Sokoloski[3] and Montana N. Williams[14]

[1]*Center for Data Intensive and Time Domain Astronomy, Department of Physics and Astronomy, Michigan State University, East Lansing, MI 48824, USA*
[2]*School of Natural Sciences, Institute for Advanced Study, Princeton, NJ 08540, USA*
[3]*Department of Physics and Columbia Astrophysics Laboratory, Columbia University, New York, NY 10027, USA*
[4]*National Radio Astronomy Observatory, P.O. Box O, Socorro, NM 87801, USA*
[5]*Center for Computational Astrophysics, Flatiron Institute, 162 5th Avenue, New York, NY 10010, USA*
[6]*Department of Physics and Astronomy, Chalmers University of Technology, Onsala Space Observatory, SE-43992 Onsala, Sweden*
[7]*School of Physics and Astronomy, University of Leicester, Leicester LE1 7RH, UK*
[8]*Department of Astronomy, University of Illinois at Urbana-Champaign, 1002 W. Green Street, Urbana, IL 61801, USA*
[9]*Department of Physics & Astronomy, Texas Tech University, Box 41051, Lubbock, TX, 79409-1051, USA*
[10]*Center for Space Science and Technology, University of Maryland Baltimore County, Baltimore, MD 21250, USA*
[11]*CRESST and X-ray Astrophysics Laboratory, NASA/GSFC, Greenbelt, MD 20771,USA*
[12]*Joint Institute for VLBI ERIC (JIVE), Oude Hoogeveensedijk 4, NL-7991 PD, Dwingeloo, the Netherlands*
[13]*Herzberg Institute of Astrophysics, National Research Council of Canada, Penticton, BC V2A 6J9, Canada*
[14]*Department of Physics, New Mexico Tech, 801 Leroy Pl., Socorro, NM 87801, USA*

Accepted 2026 September 7. Received 2026 September 2; in original form 2026 March 13

ABSTRACT

We present very long baseline interferometric (VLBI) radio imaging and *Fermi*/LAT GeV γ-ray observations of the 2019 eruption of the symbiotic recurrent nova V3890 Sgr. The VLBI imaging spans 8–51 d after the eruption, synchronous with the detected γ-rays. VLBI imaging shows the eruption begins asymmetrically on day 8 and becomes rather circularly symmetric by day 32. This morphological evolution is explained by interaction with circumstellar material (CSM) comprised of a spherical wind plus an overdensity in the orbital plane. Comparing radio images to optical line widths gives an expansion parallax distance of 6.8 kpc. In the first 32 d of eruption, VLBI images capture >80 per cent of the integrated flux implying that synchrotron emission dominates. A second peak in the VLA light curve is explained by an image on day 48 that reveals the nova shell surrounded by a diffuse synchrotron halo. The γ-rays appear around optical maximum and remain detectable for 23 d; marginally significant γ-rays reappear around day 60, concurrent with the second radio peak. Modelling indicates radio and γ-ray emission arise in distinct shock regions: γ-rays from CSM in the orbital plane, radio from the spherical CSM component. X-ray observations constrain the spherical CSM density, which is higher than in other symbiotic recurrent novae. Assuming equipartition, we estimate the fraction of the post-shock pressure in magnetic fields, ϵ_B =few $\times 10^{-3}$.

Key words: novae, cataclysmic variables – binaries: symbiotic – radio continuum: transients – gamma-rays: stars – acceleration of particles – stars: individual: V3890 Sgr.

1 INTRODUCTION

Novae are thermonuclear eruptions that occur on the surfaces of accreting white dwarfs in binary systems (J. S. Gallagher & S. Starrfield 1978; M. F. Bode & A. Evans 2008; L. Chomiuk, B. D. Metzger & K. J. Shen 2021a). The white dwarf accumulates hydrogen-rich material on its surface from the companion star, which may range from a main-sequence star to a giant. As this material builds up, the bottom layer compresses, temperature increases, and the rate of nuclear reactions increase, leading to a thermonuclear runaway, seen as an increase in luminosity (S. Starrfield, C. Iliadis & W. R. Hix 2016). The eruption blows off the accreted envelope mixed with some white dwarf material at velocities ranging from 500 to 10 000 km s^{-1} (e.g. O. Yaron et al. 2005; G. C. Anupama et al. 2013; A. Özdönmez et al. 2018). As the ejected mass is relatively small (10^{-3} to 10^{-7}M$_\odot$; R. D. Gehrz et al. 1998; O. Yaron et al. 2005), the binary system survives the

★ E-mail: molinai1@msu.edu

© The Author(s) 2026.
Published by Oxford University Press on behalf of Royal Astronomical Society. This is an Open Access article distributed under the terms of the Creative Commons Attribution License (https://creativecommons.org/licenses/by/4.0/), which permits unrestricted reuse, distribution, and reproduction in any medium, provided the original work is properly cited.

Downloaded from academic.oup.com/mnras/article/552/4/stag1851/8842644 by Chalmers tekniska högskola (Chalmers University of Technology) user on 28 October 2026

eruption and accretion can continue, accumulating hydrogen-rich matter for the next nova eruption (M. J. Darnley et al. 2014; J. Basu et al. 2025).

In some cases, multiple eruptions have been observed in the same system; these novae are called recurrent novae. The majority of novae have recurrence times longer than a human lifespan and have only had one observed eruption. However, 10 recurrent novae are well established in the Milky Way (B. E. Schaefer 2010; M. J. Darnley 2021), with an 11th recently discovered (D. Frostig et al. 2026) and several other novae claimed to have short recurrence times (J. Mikolajewska 2010; A. Pagnotta & B. E. Schaefer 2014; M. W. Healy-Kalesh et al. 2024; M. M. Shara et al. 2024). Four of the 10 well-established recurrent novae are symbiotic binaries (S. J. Kenyon 1986), including V3890 Sgr. The prevalence of giant companions among recurrent novae is often explained by accretion fed by red giant winds reaching higher rates than accretion fed by a main-sequence companion filling its Roche Lobe (H.-L. Chen et al. 2016; A. J. Kemp et al. 2021).

1.1 V3890 Sgr

V3890 Sgr is a symbiotic recurrent nova (B. E. Schaefer 2010) with an M5 III giant companion (T. E. Harrison, J. J. Johnson & J. Spyromilio 1993). It has had three observed eruptions: 2019 August 27.87 (J. Strader et al. 2019), 1990 April 27.7 (D. A. H. Buckley et al. 1990; G. C. Anupama & S. Sethi 1994), and 1962 June 2 (W. Wenzel 1990; L. T. P. Miller 1991). The recurrence time is short, only about 28 yr between eruptions. It is possible that we have missed an eruption as the nova is behind the Sun every December, and the optical light curve shows a rapid decline, $t_3 = 14$ d (J. Mikołajewska et al. 2021). The distance is constrained to 6–9 kpc (J. Mikołajewska et al. 2021), and is discussed further in Section 3.3. The mass of the white dwarf is estimated at 1.35 $M_\odot$, and the orbital period is 747.6 d (J. Mikołajewska et al. 2021).

The most recent 2019 eruption of V3890 Sgr was observed in γ-ray, X-ray, UV, optical, IR, and radio wavelengths (S. Buson, P. Jean & C. C. Cheung 2019; M. M. Nyamai et al. 2019; E. Polisensky et al. 2019; M. Orio et al. 2020; A. Evans et al. 2022; B. Kaminsky et al. 2022; J. U. Ness et al. 2022). Here, we are focused on high-resolution very long baseline interferometry (VLBI) radio observations and GeV γ-ray observations of the eruption.

Radio observations of the 2019 eruption were reported by M. M. Nyamai et al. (2023). Observations began about 7 d after discovery of the eruption and were carried out using MeerKAT and the Karl G. Jansky Very Large Array (VLA), with frequencies ranging from 1 to 37 GHz. The 5 and 7 GHz light curves peak on day 11.2 at ∼50 mJy, while the 1.26 GHz light curve peaks a bit later, on day 16.1, and at a slightly lower flux density, 44.7 mJy. M. M. Nyamai et al. (2023) concluded that the radio light curve is dominated by synchrotron emission based on brightness temperature arguments. There is a second increase in radio flux density on day 45 seen in frequency bands 1.26–7.0 GHz. This second peak in the radio light curve is difficult to explain as thermal emission (as in other novae; J. H. S. Weston et al. 2016; T. Finzell et al. 2018). This second bump has been interpreted instead as synchrotron emission resulting from interaction with circumstellar material (CSM) with a complex structure. M. M. Nyamai et al. (2023) suggest that the CSM around the nova is complex in shape, with perhaps a denser region at a distance from the white dwarf, $\sim 10^{15}$ cm.

V3890 Sgr was also detected in GeV γ-rays by the Large Area Telescope (LAT) on the *Fermi Gamma Ray Space Telescope* shortly after the start of the eruption (S. Buson et al. 2019). This makes it the third nova with a giant companion to be significantly detected by *Fermi*, joining the ranks of V407 Cyg (A. A. Abdo et al. 2010) and RS Oph (C. C. Cheung et al. 2022) (V745 Sco was also a marginal detection; A. Franckowiak et al. 2018). According to this Astronomer's Telegram on V3890 Sgr, the *Fermi* onset began at the time of optical peak, and lasted 12 d.

1.2 Shocks in Nova eruptions

This paper focuses on the shock signatures from the 2019 eruption of V3890 Sgr, in both radio and γ-ray bands. In the last decade, shocks in novae have been recognized as energetically important and key for shaping their electromagnetic emission (L. Chomiuk et al. 2021a). To date, 26 Galactic novae have been detected in GeV γ-rays by *Fermi*/LAT, which signals that novae efficiently accelerate particles to relativistic speeds through diffusive shock acceleration (P. Craig et al. 2025). Most of these novae have main-sequence companions and are surrounded by low-density environments born of conservative mass transfer (M. Ackermann et al. 2014), so the shocks are internal to the nova ejecta (L. Chomiuk et al. 2014). However, a handful of *Fermi*-detected novae have giant companions, where mass transfer is expected to be messier, and the environment is polluted by the red giant wind (A. A. Abdo et al. 2010; R. Diesing et al. 2023). In these systems, the shock is expected to be external with pre-existing CSM. This dichotomy is further supported by X-ray observations of novae; in *Fermi*-detected novae with main-sequence companions, hot shocked gas is not detected contemporaneously with γ-rays despite numerous observations with *Swift*/XRT, implying high absorption columns (T. Nelson et al. 2019; A. C. Gordon et al. 2021) or suppression of hot gas behind a radiative shock due to mixing with cooler gas (E. Steinberg & B. D. Metzger 2018; B. D. Metzger, L. Lancaster & R. Diesing 2025; S. Mitrani et al. 2025). On the other hand, novae with giant companions often show thermal X-ray emission from shocked gas from the earliest phases of their eruption (J. L. Sokoloski et al. 2006; T. Nelson et al. 2012; K. L. Page et al. 2015, 2020), implying significantly lower absorption columns.

The CSM is often modelled as a spherical wind with a r^{-2} density profile, and an equatorial density enhancement (EDE) in the orbital plane, driven by gravitational focusing of the mass-loss by the white dwarf (S. Orlando, J. J. Drake & J. M. Laming 2009; S. Mohamed & P. Podsiadlowski 2012; S. Orlando, J. J. Drake & M. Miceli 2017; S. Orlando et al. 2025). This is the scenario we have in mind in studying V3890 Sgr's 2019 eruption: external shocks between the nova ejecta and CSM, and denser interaction in the orbital plane.

1.3 This paper

Here we present high-resolution radio images and analysis of the 2019 eruption of V3890 Sgr using data obtained with the Very Long Baseline Array (VLBA) and the European VLBI Network (EVN) plus the Enhanced Multi-Element Remotely Linked Interferometer Network (e-MERLIN). We also analyse data from *Fermi*/LAT to characterize the GeV γ-ray light curve. With observations in both wavelengths, we are able to compare results, investigate the efficiency of particle acceleration and discuss the evolution of the blast and the structure of the surrounding CSM.

In Section 2, we describe the data sets under consideration. Section 3 contains analyses of the VLBA and EVN + e-MERLIN images, using them to test the origin of the radio emission, to

Downloaded from academic.oup.com/mnras/article/552/4/stag1851/8842644 by Chalmers tekniska högskola (Chalmers University of Technology) user on 28 October 2026

Table 1. VLBI and corresponding VLA observations of V3890 Sgr.

UT date	$t - t_0$ [a] (d)	Freq (GHz)	Flux ± Error (VLA) (mJy)	Flux ± Error (VLBI)[b] (mJy)	Major axis[c] (mas)	Minor axis[d] (mas)	RMS noise (μJy bm^{-1})	Panel[e]
2019 Sep 5.0	8.1	4.87	43.5 ± 2.2	37.75 ± 4.17			115	(a)
2019 Sep 5.0	8.1	8.37	44.6 ± 2.2	36.91 ± 2.37	8.4	8.0	82	(b)
2019 Sep 13.0	16.1	4.87	44.0 ± 2.2	36.42 ± 2.02			116	(c)
2019 Sep 12.9	16.0	8.37	39.9 ± 2.0	32.68 ± 1.75	13.7	13.3	58	(d)
2019 Sep 28.9	32.0	4.87	24.8 ± 1.2	24.61 ± 1.37	22.5	21.5	60	(e)
2019 Oct 15.6	48.7	4.93	17.3 ± 0.9	12.44 ± 0.64 [f]	46.0	43.2	31	(g)
2019 Oct 15.6	48.7	4.93	17.3 ± 0.9	17.15 ± 0.94 [g]	157	96	31	(h)
2019 Oct 17.9	51.0	4.87	17.3 ± 0.9	14.00 ± 0.80	34.0	31.9	22	(f)

[a]We take the start of eruption t_0 to be 2019 Aug 27.9 UT.
[b]All VLBI images were obtained with the VLBA, except the 2019 Oct 15 epoch, which was obtained with the EVN + e-MERLIN.
[c]Oriented east-west in all images, except the diffuse flux on 2019 Oct 15, when the major axis has a PA = 50°.
[d]Oriented north–south in images, except for the diffuse flux on 2019 Oct 15.
[e]Images are shown in these corresponding panels of Fig. 1.
[f]Measurements for the bright nova shell, equivalent to what is captured in VLBA images.
[g]Measurements include the diffuse emission surrounding the nova shell.

measure the magnetic field strength, and to estimate an expansion parallax distance of 6.8 kpc. In Section 4, we analyse the *Fermi* data, presenting the light curve over the first 75 d of the eruption and demonstrating a curious-but-marginal reappearance of γ-rays around the time of the second radio bump. We discuss and model our findings in Section 5, estimating the efficiency of magnetic field amplification and particle acceleration, describing efforts to simultaneously model the radio and γ-ray emission, and exploring the origin of the second bump in the radio and γ-ray light curves. We conclude in Section 6.

2 OBSERVATIONS AND DATA REDUCTION

2.1 VLBA radio observations of the 2019 eruption

High-resolution imaging observations of V3890 Sgr with the VLBA started on 2019 September 5.0 (8.1 d after start of eruption) and ended 2020 February 8 (164 d after eruption). Nine observations were obtained under VLBA project code BL267 (PI Linford). For observations taken on 2019 September 28 and October 17 in X band (center frequency 8.37 GHz) and February 8 in C band (center frequency 4.87 GHz), we were unable to properly calibrate the data. The phases were scattered and the check source when imaged was not a point source, indicating that there was an issue with the calibration, perhaps due to the southerly declination of the source and resulting low elevation of observations. We made several attempts to calibrate the data but unfortunately were unable to get usable results. Because of this, we decided to cut out these data and do not include them in any of the following plots, images, or analysis. The six observations that yielded good images are listed in Table 1. VLA observations, which are useful for determining V3890 Sgr's integrated flux density, began on August 30th (M. M. Nyamai et al. 2023). For each VLBA observation, there were near-contemporaneous VLA observations at 5 and 7 GHz.

The September 5 and September 13 observations included both 4.87 and 8.37 GHz, with observations switching between bands on average every 42 min. The September 28 and October 17 observations only had usable data at 4.87 GHz. The phase reference calibrator was J1820−2528, and the check source was J1819−2036. For the final two observations, a fringe finder (J1924−2914) was included. Each observation has 4 spectral windows, each 128 MHz wide, resulting in a total bandwidth of 512 MHz. There are 128 spectral channels per spectral window. All data were obtained in full Stokes mode. The exposure time of each epoch was about 1.8 h on V3890 Sgr, except for the October 17th 4.87 GHz observation, which was 3.6 h. On the September 5 observation, Mauna Kea did not join until about 2 h after the start of the observation. On the September 28 observation, Brewster was not recording data.

After flagging poor data and radio frequency interference on the calibrator scans, we noticed the phase calibrator J1820−2528 showed complex structure, so we split it into its own fits file and loaded it into DIFMAP (M. C. Shepherd 1997) in order to improve our model. There, we iteratively self-calibrated and imaged the calibrator data, recovering some diffuse flux surrounding a point-like source. This improved model was loaded back into AIPS and then used in the calibration process.

The data were calibrated using standard routines in AIPS 31DEC22 (E. W. Greisen 2003). Instrumental delay calibration and bandpass calibration were performed using J1820−2528 for the observations taken on September 5 and 13. For observations taken on September 28 and October 17 both J1820−2528 and J1924−2914 were used. Global fringe fitting was then carried out with solution intervals of 1 min over the course of the observation. Again, for the last two observations J1924−2914 was included in the global fringe fitting. Flux calibration was carried out using VLBAAMP in AIPS. In AIPS phase and amplitude self-calibration were performed on the calibrator with a solution interval of 0.5 and 1 min, respectively.

The science target was then flagged, calibrated, and split. It was exported into DIFMAP and imaged in Stokes I. We used RADPLOT to further flag the data before cleaning the image. Natural weighting was used for all epochs. Images of all VLBA observations were made with untapered data to obtain maximum angular resolution. We boxed regions with significantly higher flux density than the background and used the CLEAN algorithm to clean the image. This was done repeatedly, applying phase SELFCAL of decreasing integration intervals until we reached a solution interval of 2 min. The final image was viewed in MAPL CLN.

2.2 EVN plus e-MERLIN observations

To reveal more details about V3890 Sgr as it expands and fades, we also performed real-time *e*-VLBI observations (project code:

Downloaded from academic.oup.com/mnras/article/552/4/stag1851/8842644 by Chalmers tekniska högskola (Chalmers University of Technology) user on 28 October 2026

RY008, PI: Jun Yang) with the EVN plus e-MERLIN at 4.9 GHz on 2019 October 15 (48.7 d after the start of eruption). The target-of-opportunity observations lasted about four h (UT: 14:30–18:30). The participating stations were Jodrell Bank, Westerbork, Effelsberg, Medicina, Onsala, Yebes, Hartesbeesthoek, Zelenchukskaya, Irebene, Cambridge, Darnhall, Pickmere, Defford, and Knockin. The observations used the default frequency setup at C band for the EVN (16 subbands in dual polarization, 32 MHz per subband, 2-bit quantization) and e-MERLIN (2 subbands in dual polarization, 64 MHz per subband, 2-bit quantization) stations.

We used a different source, J1828−2417, as the phase-referencing calibrator during the EVN and e-MERLIN observations of V3890 Sgr. The calibrator is only half degree apart from V3890 Sgr and has a compact core-jet VLBI structure with a correlation amplitude of 21 mJy on the long baselines at 8.4 GHz. The nodding observations used a cycle time of 3 min: 20 s for the calibrator, 100 s for the target, and 60 s for the antenna slewing time. To derive the relative position of J1828−2417 with respect to J1820−2528, i.e. the bright calibrator used in the above VLBA observations, we also observed the pair of calibrators for 11 phase-referencing cycles.

The correlation data were calibrated in AIPS 31DEC22 (E. W. Greisen 2003). When the visibility data were loaded into AIPS discs, we ran AIPS task ACCOR to slightly correct cross-correlation amplitudes. Before general *a priori* amplitude calibration, the antenna system temperature data were significantly smoothed to minimize their random errors. When antenna system temperatures and gain curves were not available, we used nominal system equivalent flux densities and a flat gain curve to do *a priori* amplitude calibration. The task TECOR was used to remove ionospheric dispersive delays calculated according to maps of total electron content provided by Global Positioning System (GPS) satellite observations. The phase errors resulting from the antenna parallactic angle variations were removed. We corrected the instrumental phases and delays across the subbands via running fringe-fitting with the data from the bright fringe finder J1800+3848. After removing the instrumental phase errors, all subband data of were combined to run more accurate fringe fitting with a solution interval of 20 s. The most sensitive telescope Effelsberg was used as the reference station. The solutions were also applied by two-point linear interpolation from J1828−2417 to V3890 Sgr and J1820−2528. The phase connections were also quite smooth at all stations. Bandpass calibration was also performed using the fringe finder J1800+3848.

The deconvolution was performed in DIFMAP (M. C. Shepherd 1997). The calibrator J0834−0417 shows a one-sided core-jet structure with a total flux density of ∼38 mJy at 4.93 GHz. With the input image, we re-ran the fringe-fitting and the amplitude and phase self-calibration in AIPS. All of these solutions were also transferred to the target data by linear interpolation. The target V3890 Sgr was imaged without self-calibration. The low-elevation data in the first and last hours were excluded in the imaging process. The small positional offset of the weak calibrator J1828−2417 was calculated with respect to the bright calibrator J1820+2528, and was corrected in the VLBI map of V3890 Sgr.

2.3 *Fermi*/LAT γ-ray observations of the 2019 eruption

V3890 Sgr was observed at GeV γ-ray energies using *Fermi*/LAT. For our γ-ray analysis of V3890 Sgr, we used FERMITOOLS (version 2.4.0). Our analysis is based on the binned likelihood tutorial provided by the *Fermi* team.[1] We begin by selecting events based on their class and type, selecting only events with `evclass = 128` and `evtype = 3`. We also select for good time intervals using the logical expression `(DATA_QUAL>0)&&(LAT_CONFIG== = 1)`. The selected observations contain all the Pass 8 (P8R3_V3) γ-ray events from 100 MeV to 300 GeV within 10 degrees of the nova. We use a model including all the known sources in the 4FGL-DR3 catalogue (S. Abdollahi et al. 2022) within 20 degrees of V3890 Sgr. Also included are the Galactic diffuse emission and the isotropic emission models (i.e. `gll_iem_v07` and `iso_P8R3_SOURCE_V3_v1`). A point source model for V3890 Sgr is added as well, assuming a power-law spectrum with an exponential cut-off, as is frequently used to model the γ-ray spectra of novae (A. Franckowiak et al. 2018). This spectral model is shown in equation (1), where N_0 is a normalization parameter, γ_1 is the power-law index, E_c is the energy cut-off, and E_0 is an energy scale fixed to 200 MeV.

$$\frac{\mathrm{d}N}{\mathrm{d}E} = N_0 \left(\frac{E}{E_0}\right)^{-\gamma_1} e^{-\frac{E}{E_c}}, \tag{1}$$

We analysed the *Fermi*/LAT data to obtain V3890 Sgr's GeV γ-ray flux, fitting this model to data ranging from 2 d before the optical peak to 20 d after the peak. This 22-d window was used to obtain the average flux for this nova, and to obtain spectral parameters. As is typical for a *Fermi* analysis, we estimate our detection significance using the test statistic, which is −2 times the likelihood ratio between the best-fitting model including the nova and a background only model. This can be converted to a typical significance level by taking the square root of the test statistic. In our case, this time window yields a $> 5\sigma$ detection, making the detection of γ-ray emission from V3890 Sgr unambiguous. Due to the relatively large distance, and correspondingly small observed γ-ray flux of V3890 Sgr, the spectral parameters remain highly uncertain. We recover a spectral index of $\gamma_1 = 1.4 \pm 1.8$ with a cut-off energy of 2 GeV, though the spectral model is not well constrained.

After obtaining the average flux and associated test statistic for V3890 Sgr, we built a light curve starting 60 d before the optical peak, with each point using 15 d of data (as in A. Franckowiak et al. 2018). The resulting light curve is discussed in Section 4. Throughout this light curve, we fix the spectral parameters to a set that is typical for the γ-ray emission from novae, assuming a power-law index of 1.9 and a cut-off energy of 4.3 GeV (A. Franckowiak et al. 2018). In many of the light-curve bins the data are insufficient to meaningfully constrain the spectral parameters, so the only model parameter for V3890 Sgr allowed to vary is the normalization.

2.4 *Swift* XRT X-ray observations

X-ray telescope (XRT) observations with the *Neil Gehrels Swift Observatory* began about 0.7 d after eruption, revealing a bright hard X-ray source (K. V. Sokolovsky et al. 2019). Data were taken from August 28 to September 5, took a brief hiatus for proximity to the Moon, and proceeded at decreasing cadence from September 10 until V3890 Sgr entered solar conjunction on November 11. Once the nova was no longer blocked by the Sun, observations resumed on 2020 February 17 until May 4.

[1] https://fermi.gsfc.nasa.gov/ssc/data/analysis/scitools/binned_likelihood_tutorial.html

Downloaded from academic.oup.com/mnras/article/552/4/stag1851/8842644 by Chalmers tekniska högskola (Chalmers University of Technology) user on 28 October 2026

Swift data were processed using HEASOFT and the most recent calibration files available for late 2019. Here, we use the same spectral fits as K. L. Page et al. (2019) for constraining the X-ray emission at the epochs of our VLBI imaging. On days 7.7 and 51.4, the spectrum is fit with a single optically thin thermal component (i.e. APEC, which represents hot shocked gas). On day 15.5, the fit is improved by the addition of a second APEC component and also a blackbody component (which represents the supersoft source). By day 31.9, the supersoft source had faded, but the optically thin thermal emission is still better fit by two APEC components than one. Absorption is held fixed at $N_H = 5.1 \times 10^{21}$ cm^{-2}. The APEC parameters (kT and normalization) are listed in Table 3.

2.5 Optical spectroscopy of the 2019 eruption

As an additional constraint on the ejecta velocities in V3890 Sgr, we considered optical spectroscopy of the 2019 eruption obtained using the Small and Moderate Aperture Research Telescope System (SMARTS) 1.5 m telescope and its CHIRON optical spectrograph (F. M. Walter et al. 2012). The observations covered the wavelength range 4082-8770 Å with a resolution of $R = 27\,800$. Observations post eruption began on 2019 August 28 and ended 2019 November 4 with some spectra obtained pre-eruption.

3 VLBI RADIO IMAGE ANALYSIS

Our VLBA radio images of V3890 Sgr's 2019 eruption are plotted in panels (a–f) of Fig. 1 in J2000 equatorial coordinates. The EVN + e-MERLIN image is shown in panels (g) and (h) of Fig. 1. In each image, the position of the binary star as derived from *Gaia* Data Release 3 (Gaia Collaboration et al. 2016, 2023) is marked using a white dot and error bars; the *Gaia* position was corrected for proper motion to the observation time of each image. The *Gaia* position at the average observing epoch (2019.81) is RA = 18h30m43.2824s and Dec. = −24°01′08.″988, and the error bars are smaller than the marker and are not visible in the images.

The background RMS noise was found in DIFMAP by calculating statistics on a blank image region away from the nova. The rms noise levels in the 8.37 GHz images were 58–82 μJy beam^{-1} and the noise values in the VLBA 4.87 GHz images were 22–116 μJy beam^{-1}. The specific image noise values are listed in Table 1. The rms noise in the 4.93 GHz EVN + e-MERLIN image is 31 μJy beam^{-1}. The image RMS values were used to set the contour levels in the images to −1.5, 1, 3, 5, and 7σ (Fig. 1). These noise levels can be compared with the theoretical thermal noise of the VLBA, as calculated using the EVN calculator. This led to theoretical noise estimates of 18.1 μJy beam^{-1} at 8.37 GHz with the VLBA, 15.4 μJy beam^{-1} at 4.87 GHz with the VLBA, and 13.0 μJy beam^{-1} for the EVN + e-MERLIN observation. It is not unusual for VLBI images to have observed noise values several times that theoretically expected, and reaching theoretical noise was made unusually difficult by the low elevation of V3890 Sgr as observed by these radio facilities.

All VLBA images are centered at the same location (RA = 18h30m43.2826s, Dec = −24°01′08.″990) with the same map size (2048 pixels on a side) and pixel size (0.15 mas). For the 4.87 GHz VLBA images, the average FWHM resolution is $B_{\rm maj} = 4.5$ mas along the major axis and $B_{\rm min} = 1.7$ mas along the minor axis with an average position angle of PA = −1.3°. The 8.37 GHz images have an average resolution $B_{\rm maj} = 2.7$ mas and $B_{\rm min} = 1.0$ mas. The 4.93 GHz EVN + e-MERLIN image is restored with a symmetric beam of FWHM = 10 mas.

3.1 Morphology and evolution

The images in Fig. 1 show how the shape of the nova changes over time. Eight days after eruption, we see an elliptical compact source offset to the east – likely a lobe of a bipolar outflow – and another small region to the west of the source center [panels (a) and (b) of Fig. 1]. This fainter western component is more apparent in the 8.37 GHz image than the 4.87 GHz image (panel b compared with panel a). This likely implies that the western structure is absorbed by intervening CSM in this first epoch.

Sixteen days after eruption, radio emission from V3890 Sgr has become more spread out [panels (c) and (d) of Fig. 1], and both lobes are now more apparent. In the 4.87 GHz image, the brightest region remains the eastern lobe. The small structure beneath the nova, located at Dec of about −24:01:09.00 in panel (c), is likely an artefact as we do not see it in later epochs. At 8.37 GHz, the radio emission is noisier, as expected from the higher angular resolution sampling the nova with more synthesized beams. The eastern and western lobes are of more comparable brightness at 8.37 GHz, implying that optical depth continues to affect the western lobe at 4.87 GHz.

The shape of the early radio emission could be explained if the CSM is composed of a spherical wind and a region of increased density in the orbital plane, (i.e. the EDE; R. Walder, D. Folini & S. N. Shore 2008; S. Mohamed, R. Booth & P. Podsiadlowski 2013; R. A. Booth, S. Mohamed & P. Podsiadlowski 2014; S. Orlando et al. 2017). Our images constrain the position angle of the EDE to be in the range, 0 to −15° (oriented roughly up–down in Fig. 1). The EDE impedes expansion in the north–south direction and confines the ejecta into two lobes oriented mostly east–west. The lobes being imaged in VLBA suggest that the synchrotron emission is coming from the lobes and not the central disc. The synchrotron emission would then be coming from interactions with the spherical component of the CSM. The inclination angle of the nova is well constrained to be 67-69° by J. Mikołajewska et al. (2021), and our VLBA imaging shows that the eastern side is tilted towards us, while the western side is tilted away from us and undergoes more absorption from the EDE in early imaging epochs.

During the third epoch, 32 d after eruption (panel e of Fig. 1), the radio-emitting region continues to expand and now looks quite symmetric east–west. The nova no longer looks so bipolar, and has similar dimensions north–south and east–west (Table 1). There are significant deconvolution artifacts visible around the nova in this epoch (visible as blotches at top-right and bottom-left in panel e); these should be disregarded.

The time period of day 48–51 is imaged by both the VLBA and EVN; while the VLBA has higher resolution, EVN + e-MERLIN is more sensitive to lower surface brightness emission. The VLBA image from this last epoch is quite noisy, implying that the surface brightness of the radio emission has dropped [panel (f) of Fig. 1]. The EVN + e-MERLIN image, however, captures more of the flux at higher significance, and now shows that the nova is brighter along the north–south axis: a ∼ 90° flip from what was observed earlier in the eruption (panel g of Fig. 1). The radio-emitting shocks therefore seem to be primarily interacting with the EDE at this late epoch.

The EVN + e-MERLIN image from day 48 also shows significant diffuse radio flux external to the primary nova shell (panel h

Downloaded from academic.oup.com/mnras/article/552/4/stag1851/8842644 by Chalmers tekniska högskola (Chalmers University of Technology) user on 28 October 2026

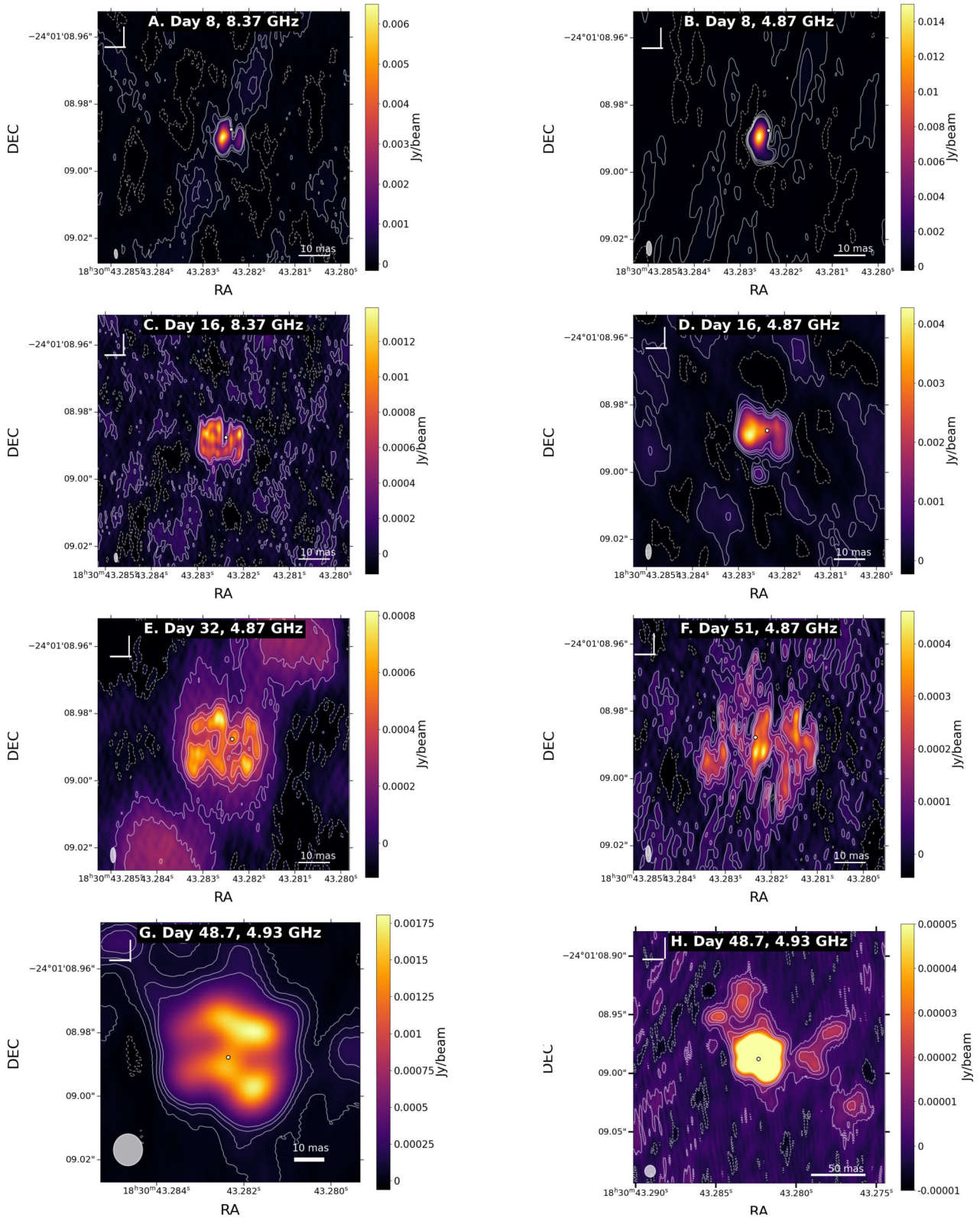


Figure 1. VLBI radio images of the 2019 eruption of V3890 Sgr. The top two panels, (a) and (b), show 4.87 and 8.37 GHz VLBA images on day 8.1. The second row – panels (c) and (d) – show 4.87 and 8.37 GHz VLBA images on day 16. The third row shows 4.87 GHz VLBA images from day 32.0 (panel e) and day 51.0 (panel f). The bottom row show the EVN + e-MERLIN image from day 48.7; panel (g) is on the same scale as panels (a–f), while panel (h) zooms out to show a larger field of view. In each panel, the contour levels are set to -1.5, 1, 3, 5, and 7σ (see Table 1 for σ values). The white dot is located at the *Gaia* position of V3890 Sgr. In the upper left corner is a compass showing the North (up) and East (left) directions. The synthesized beam is plotted in the bottom left corner. The field of view is 80 mas across for panels (a–g), and 225 mas across for panel (h). Note that each panel has its own color scale, as denoted in its colour bar.

Downloaded from academic.oup.com/mnras/article/552/4/stag1851/8842644 by Chalmers tekniska högskola (Chalmers University of Technology) user on 28 October 2026

Table 2. Properties derived from VLBA radio images of V3890 Sgr.

Day	Freq (GHz)	l [a] (cm)	$B_{K_0=40}$ [b] (G)	$B_{K_0=100}$ [b] (G)	v_s (km s^{-1})	$\epsilon_B(K_0=40)$ [c]	$\epsilon_B(K_0=100)$ [c]
8.1	8.37	8.0×10^{14}	0.16 (0.27)	0.20 (0.35)	5940[d]	4.5×10^{-4} (1.3×10^{-3})	7.0×10^{-4} (2.1×10^{-3})
16.0	8.37	1.4×10^{15}	0.09 (0.15)	0.11 (0.19)	3970[e]	8.4×10^{-4} (2.2×10^{-3})	1.3×10^{-3} (3.7×10^{-3})
32.0	4.87	2.2×10^{15}	0.05 (0.08)	0.06 (0.11)	3130[f]	1.4×10^{-3} (3.5×10^{-3})	2.0×10^{-3} (6.6×10^{-3})
51.0	4.87	3.2×10^{15}	0.03 (0.05)	0.04 (0.06)	3390[g]	1.1×10^{-3} (3.0×10^{-3})	1.9×10^{-3} (4.3×10^{-3})

[a]Diameter of the radio emission, assuming a distance of 6.8 kpc.
[b]Magnetic field estimated using $\alpha=-0.7$. Bracketed values result from using $\alpha=-0.55$.
[c] ϵ_B estimated assuming v_s from this table and n_e from Table 3. Bracketed values are the result of using the magnetic field strengths using $\alpha=-0.55$
[d]Velocity between day 0–8.1, representing the geometric mean of the major and minor axes.
[e]Velocity between day 8.1–16.0.
[f]Velocity between day 16.0–32.0.
[g]Velocity between day 32.0–51.0.

of Fig. 1). This emission is patchy, elongated, and asymmetrically distributed around the nova shell, with a position angle of $\sim 50^\circ$.

Compared with RS Oph's 2021 eruption, our VLBA images appear to be missing a central disc component. In addition to this compact central component, RS Oph shows a bi-lobed structure similar to V3890 Sgr, with one lobe being initially fainter and then increasing in brightness over time, which is attributed to absorption by an EDE (U. Munari et al. 2022; R. Lico et al. 2024). However, RS Oph remains more elongated/bipolar in later epochs (64–65 d after explosion), while V3890 Sgr exhibits more circular symmetry in our later imaging epochs (Fig. 1). V407 Cyg – a 2010 nova that erupted in a longer-period symbiotic binary with an asymptotic giant branch companion and the first nova detected in GeV γ-rays (A. A. Abdo et al. 2010) – was imaged with VLBI 20 to 203 d after eruption. Images revealed an expanding elliptical shell with no central brightening (M. Giroletti et al. 2020). They also exhibit radio emission at larger radii than can be attributed to the nova eruption (M. Giroletti et al. 2020), perhaps similar to the extended diffuse emission we observe in V3890 Sgr with the EVN + e-MERLIN.

3.2 Angular size as a function of time

We estimated the size of the radio emission from our VLBI images. In the first two epochs, we use the 8.37 GHz images for size determination, as they are both higher resolution and less affected by absorption than the 4.87 GHz images. As the source morphology is complex and not well described by e.g. a Gaussian, we do not fit the source with parametric models in the uv plane; instead, we directly estimate the source size from the image.

For the first epoch, the size of the nova was determined using JMFIT in AIPS by fitting two Gaussians to the nova. Both lobes of the nova were resolved, so we used the deconvolved sizes of the components to estimate the 2σ radii of the Gaussians, and then measured the distance between the centres of the Gaussians to get the distance between the two lobes. This was all added together to get the full diameter of the source along the major (roughly east–west) axis. The diameter of the nova along its minor axis was the average of the two deconvolved Gaussian widths in the ∼north–south direction.

For the remaining VLBA epochs, the size was determined by measuring the diameter of 3σ contours in CARTA.

In the EVN + e-MERLIN image, there is significant diffuse flux external to the nova shell, and we estimated the size in two different ways: the dimensions of the nova shell estimated from 5σ contours in CARTA, and the larger dimensions of the diffuse flux estimated from 3σ contours. We note that the dimensions of the nova shell estimated from the EVN image are significantly larger than in the VLBA image from day 51 (mean diameter of 44.5 mas, compared to 32.9 mas). This could be caused by a poorly measured diameter in the noisy VLBA image or the lower resolution of the EVN image. We note that if we use the EVN dimensions of the nova shell, we find that the expanding shell would have had to significantly accelerate between day 32 and 48 (Section 3.3), which seems unlikely. We therefore conclude that the EVN dimensions of the nova shell are likely affected by the lower resolution of this image. As the EVN image and day 51 VLBA image yield similar fluxes for the nova shell, but the VLBA image better hones in on the nova shell, we use the VLBA image for estimating the shock velocity and magnetic field (Table 2).

The major and minor axes are listed in Table 1. Generally, the major axis of the nova shell is oriented east–west and the minor axis north–south, although we note that the source is not greatly elongated in the east–west direction in any of the epochs.

3.3 Velocities and expansion-parallax distance

If we assume a distance of 9 kpc to V3890 Sgr, as suggested by J. Mikołajewska et al. (2021) based on the assumption that the red giant companion is Roche-lobe filling, the diameter of V3890 Sgr's VLBA emission would be 1.1×10^{15} cm on day 8, growing to 4.7×10^{15} cm on day 51. This implies remarkably high expansion velocities of 8080 km s^{-1} over the first 8 d, and ∼5000 km s^{-1} over the following 43 d.

To test if these high expansion velocities are plausible in V3890 Sgr, we inspected Hα line profiles as observed by SMARTS/CHIRON. Six epochs of Hα line profiles of the 2019 eruption are plotted in Fig. 2. The full width at zero intensity (FWZI) was estimated for each of the Hα emission lines using SPECPLOT in IRAF. To measure the FWZI, we estimated the continuum level of the data and measured where the H α emission line met that continuum level.

A spectrum obtained more than a year before the 2019 eruption shows a very narrow Hα emission line with no extended wings. This emission emanates from the circumbinary material, ionized by the accreting white dwarf. One day following eruption, the Hα line shows a much broader emission line with a remnant of the narrow emission line superimposed (implying the presence of unshocked circumstellar material; centered at $v=-131$ km s^{-1}). While the bulk of the emission is confined to ±5000 km s^{-1}, there may be faint wings on day 1 that extend to about ±9600 km s^{-1}. However, these wings are very faint, and sensitive to

Downloaded from academic.oup.com/mnras/article/552/4/stag1851/8842644 by Chalmers tekniska högskola (Chalmers University of Technology) user on 28 October 2026

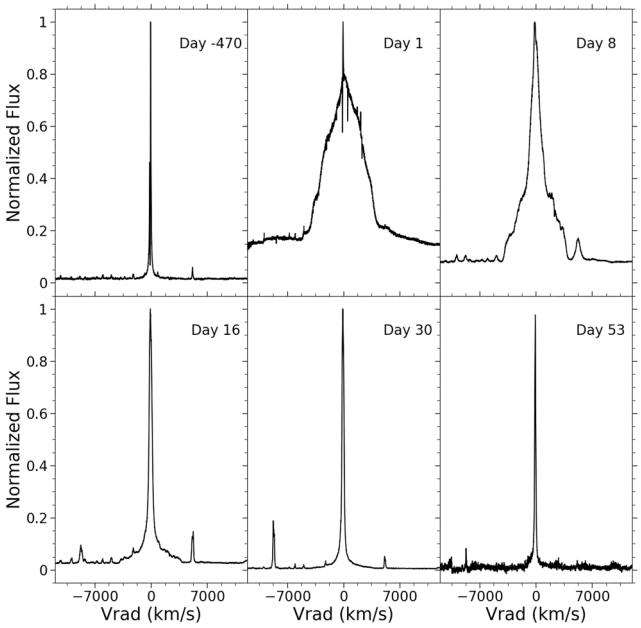


Figure 2. The H α emission-line profiles 470 d before V3890 Sgr's 2019 eruption and 1, 8, 16, 30, and 53 d after the eruption.

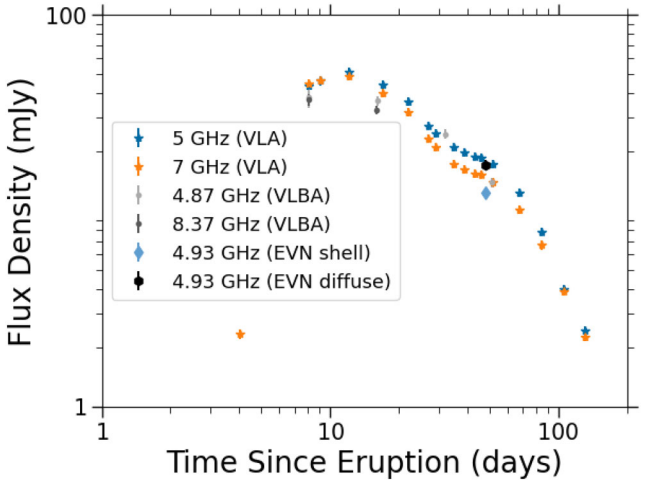


Figure 3. Integrated flux densities from our VLBA observations and the EVN + e-MERLIN observation as a function of time following V3890 Sgr's 2019 eruption, compared to the VLA light curve in similar frequency bands (VLA data published in M. M. Nyamai et al. 2023).

vagaries of continuum fitting, so we are not certain how reliable the presence of 9600 km s^{-1} gas is in V3890 Sgr. Prior to the eruption, there is no evidence of these extended wings. By day 8, the narrow component has broadened, and the broad wings have disappeared, giving the profile a near-triangular shape. Although a He I line at 6678 Å makes it difficult to measure the edge of the Hα line profile, we estimate it converges with the continuum around $\pm$4300 km s^{-1}. On day 16, the narrow component is very strong compared to the broad component, and the Hα line reaches $-$3840 km s^{-1} and +3650 km s^{-1}, indicating that the expansion is slowing. The broad component of the Hα line has further narrowed by day 30 with HWZI $v = 2520$ km s^{-1}. By day 53 the line width has decreased to about $v = \pm 1440$ km s^{-1}.

These spectroscopic velocities are lower than what is implied by our VLBA images, if we take a distance of 9 kpc. J. Mikołajewska et al. (2021) convincingly argue based on Na ID absorption lines that the distance to V3890 Sgr is at least 6 kpc, and a distance of about 9 kpc is likely an upper limit, as it assumes the red giant companion completely fills its Roche Lobe. We combine the spectroscopic velocities and our VLBA imaging to estimate expansion parallax distances, taking the expansion in the north–south direction, as V3890 Sgr is viewed relatively edge-on ($i \approx 68°$; J. Mikołajewska et al. 2021) and our imaging shows the orbital plane is oriented roughly north–south, so the radial velocity will more closely mirror the north–south expansion than east–west. Assuming that the emission began as a point source on day 0 and expanded to a diameter of 7.9 mas by day 8.1, we find a distance of 11.4 kpc if the 9600 km s^{-1} broad wings are reliable, and a distance of 5.9 kpc if the radio emission is characterized by expansion of 5000 km s^{-1}, more in line with the bulk of the emission-line flux. Between days 8 and 16, we estimate an expansion parallax distance of 6.6 kpc (for an average spectroscopic velocity of 4000 km s^{-1} during this time). Between days 16 and 32, we find 6.9 kpc for an average velocity of 3130 km s^{-1} during this time. Choosing to disregard the first epoch due to ambiguity with the FWZI measurement, we prefer a distance of 6.8 kpc to V3890 Sgr, and use this throughout the rest of this paper. Velocities estimated from our VLBA images, taking $d = 6.8$ kpc and the geometric mean of the major and minor axis of V3890 Sgr, are listed in Table 2.

At this distance, the dimensions of the diffuse radio emission detected by EVN + e-MERLIN on day 48 are 8×10^{15} cm by 5×10^{15} cm. If this material was launched on day 0 of the 2019 eruption, it would have needed to expand at $\sim$15 000 km s^{-1}, much faster than is observed in V3890 Sgr (or in any nova that we know). We therefore conclude that this diffuse emission was caused by a relativistic tracer, like photons or cosmic rays, escaping the nova shell and interacting with the environment. We discuss this scenario more in Section 5.4.

3.4 Fraction of flux 'resolved out' by VLBA

In Fig. 3, the VLA light curve, which measures V3890 Sgr's integrated radio flux density, is plotted using stars and compared to the VLBI light curve plotted as dots. The total flux density of V3890 Sgr in our VLBA and EVN + e-MERLIN images is found by boxing a region around the nova in CARTA. We then estimated the associated uncertainty by determining how many synthesized beams fit into this region, and multiplying the image rms noise by the square root of this number of beams. We added this uncertainty in quadrature with an estimated flux calibration error of 5 per cent, as all frequency bands are below 10 GHz. The resulting flux densities and errors are listed in Table 1.

We see the VLBA light curve is brightest during our first epoch on day 8, and the 4.87 GHz flux density then declines with a power-law slope of -0.91 ± 0.45 (excluding the EVN point that detects the diffuse flux). The VLA light curves peak 11 d after discovery; if we measure the power-law slope of the 5.0 GHz band from day 9 to day 51 we find a shallower decline than VLBA with power-law slope of -0.67 ± 0.05.

The VLBA observations appear to capture most of the flux density seen in the VLA observations. On day 8 the VLBA captures 87 per cent of the flux density in 4.87 GHz and on day 16 the VLBA captures 83 per cent. This confirms that the radio emission is synchrotron-dominated, as the VLBA is not sensitive to thermal

Downloaded from academic.oup.com/mnras/article/552/4/stag1851/8842644 by Chalmers tekniska högskola (Chalmers University of Technology) user on 28 October 2026

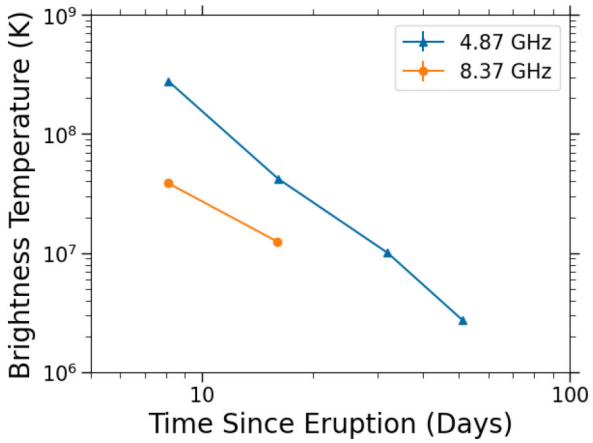


Figure 4. Brightness temperature measurements as a function of time following V3890 Sgr's 2019 eruption, measured from our VLBA images in 4.87 GHz (plotted as blue triangles) and 8.37 GHz (plotted as orange circles).

emission (the theoretical 3σ brightness temperature sensitivity of the VLBA is 3.1×10^5 K at 4.87 GHz and 3.5×10^5 K at 8.37 GHz, for our exposure times; equation 2).

However, the second bump in the VLA light curve, which happens around day 50, is missed by our day 51 VLBA image, detecting only 13.9 mJy of the 17.3 mJy integrated and explaining the steeper decline of the VLBA light curve, compared to VLA. We do note the appearance of two significant compact flux components near the center of the nova in our Day 51 image (panel f of Fig. 1). However, these two components have a combined flux of 1.8 ± 0.13 mJy, which is not enough to explain the increase in flux density in the VLA light curve around this time.

The flux density measured from the nova shell in the day 48 EVN+e-MERLIN image is similar to the day 51 VLBA image, at 12.4 mJy, but EVN + e-MERLIN recovers significant diffuse flux extended over ∼0.1 arcsec, which rivals the integrated flux, at 17.2 mJy. We conclude that the origin of the second radio bump is not caused by a brightening at the shock front (as proposed by M. M. Nyamai et al. 2023), but instead by an enhancement of diffuse radio emission upstream of the shock front. We consider possible physical explanations for this emission in Section 5.4.

3.5 Brightness temperature

The brightness temperature was calculated from our VLBA images of the nova shell, assuming a source with a Gaussian shape and the relation from J. Wrobel & R. Walker (1999):

$$T_{\rm B} = 1224\,{\rm K}\,\frac{S_\nu}{\rm mJy}\left(\frac{\nu}{\rm GHz}\right)^{-2}\left(\frac{\theta_{\rm maj}\,\theta_{\rm min}}{\rm arcsec^2}\right)^{-1}. \quad (2)$$

Here, ν is the frequency of the observation, S_ν is the flux density at that frequency, $\theta_{\rm maj}$ is the FWHM major axis of the source, and $\theta_{\rm min}$ is the FWHM minor axis. In this case, we estimated the diameter of V3890 Sgr from 3σ contour levels, as listed in Table 1.

Fig.4 plots the calculated brightness temperature as a function of time following the 2019 eruption. The 4.87 GHz brightness temperature starts at 2.8×10^8 K on day 8 and declines to a value of 2.2×10^6 K by day 51. The 8.37 GHz brightness temperature starts lower at a value of 3.9×10^7 K and declines to 1.2×10^7 K on day 16. At all times, the brightness temperature is high, staying well above a thermal expectation of $\lesssim 5 \times 10^4$ K (L. Chomiuk et al. 2021b). These $T_{\rm B}$ estimates are consistent with the conclusion in the previous subsection that the vast majority of the flux is synchrotron emission.

M. M. Nyamai et al. (2023) estimated the brightness temperature of V3890 Sgr from VLA observations of the integrated flux, by assuming a spherically symmetric shell expanding at a constant velocity of 4200 km s^{-1} at a distance of 9 kpc. The flux densities used were from the 1.28 GHz VLA observations. Our brightness temperature measurements are similar to M. M. Nyamai et al. (2023) on day 8 (2.8×10^8K vs their $\sim 2.5 \times 10^8$ K). However, our brightness temperature decreases much faster (51 d after eruption we have a value 2.2×10^6 K vs their 2×10^7 K). This difference can partially be explained by the negative spectral index and the difference in frequencies used to estimate $T_{\rm B}$. Additionally, we assume a smaller distance than M. M. Nyamai et al. (2023), and our initial velocity measurement is faster and declines more rapidly than the modeled velocity used in M. M. Nyamai et al. (2023). Our VLBA estimates of $T_{\rm B}$ are made directly from images, and are therefore more reliable than those estimated from integrated fluxes relying on assumptions about the emitting region size.

We also estimate the brightness temperature of the diffuse flux detected by the EVN + e-MERLIN on day 48 (panel (h) of Fig. 1). The emission is patchy, and peaks at 0.27 mJy beam^{-1}, which corresponds to a peak brightness temperature of 1.3×10^5 K. Such a high surface brightness makes it unlikely to be thermal emission, as might be expected if circumstellar material is photoionized by the nova; in this case, we would expect $T_{\rm B} \approx 10^4$ K. The relatively high brightness temperature of the diffuse emission and spectral index of the second radio bump (Section 3.7) make it likely that the diffuse emission is synchrotron in origin.

3.6 Magnetic field strength

The magnetic field strength in V3890 Sgr's synchrotron-emitting nova shell was calculated using the revised equipartition formula from R. Beck & M. Krause (2005):

$$B_{\rm eq} = \left(\frac{4\pi(1-2\alpha)(K_0+1)I_\nu E_{\rm p}^{1+2\alpha}(\nu/2c_1)^{-\alpha}}{(-2\alpha-1)c_2 l c_4}\right)^{\frac{1}{3-\alpha}}. \quad (3)$$

Here, K_0 is the proton-to-electron number density ratio amongst the relativistic particles, α is the radio spectral index defined as $S_\nu \propto \nu^\alpha$, I_ν is the synchrotron intensity at frequency ν, $E_{\rm p}$ is the proton rest energy (938.26 MeV), and l is the path-length through the synchrotron-emitting region. $c_1 = 6.264 \times 10^{18}$ erg^{-2}s^{-1}G^{-1} and $c_4 = (2/3)^{(\alpha+1)/2}$, as defined in R. Beck & M. Krause (2005) in Appendix A. c_2 is defined in R. Beck & M. Krause (2005): for an $\alpha = -0.7$, $c_2 = 1.016 \times 10^{-23}$erg G^{-1} sterad $^{-1}$.

The spectral index of V3890 Sgr is relatively flat compared to other astrophysical synchrotron sources. On Day 16, we estimate $\alpha = -0.25$ from our VLBA images. Even at late times, the spectral index converges to $\alpha \approx -0.4$ (M. M. Nyamai et al. 2023). However, equation (3) is only valid for α values steeper than -0.5, so we consider two spectral index values to give a sense of how B varies with assumed α. We consider $\alpha = -0.7$, as is typical for other synchrotron-emitting astrophysical shocks (e.g. K. W. Weiler et al. 2002; D. A. Green 2019) and $\alpha = -0.55$ which approximates most closely the measured spectral index in V3890 Sgr. It is quite possible that the true underlying spectrum is flatter yet than $\alpha = -0.55$, but we use the difference in B fields derived from $\alpha = -0.55$ and -0.7 to give a sense of the amplitude of uncertainty. I_ν was found by dividing the measured flux density

Downloaded from academic.oup.com/mnras/article/552/4/stag1851/8842644 by Chalmers tekniska högskola (Chalmers University of Technology) user on 28 October 2026

by the angular area of the nova, measured from our VLBA images. We set K_0 to be 40 and 100; $K_0 = 100$ comes from measurements of local Galactic cosmic rays and $K_0 = 40$ is expected for strong shocks (R. Beck & M. Krause 2005). The path length l takes a distance of 6.8 kpc and the estimates of the minor axis angular size from Table 1.

The resulting magnetic field estimates are listed in Table 2. Values for $\alpha = -0.7$ are listed first, followed by values for $\alpha = -0.55$ in brackets. The values are a factor of $\sim$1.7 higher for $\alpha = -0.55$. For day 8 and 16, we only considered the eastern VLBA component, as the western component is likely affected by absorption. On day 8 the magnetic field is 0.27 G (for $K_0 = 40$ and $\alpha = -0.55$) and diminishes to 0.05 G by day 51. For $K_0 = 100$ on day 8 the magnetic field is slightly higher at 0.35 G and declines to 0.06 G by day 51. We take the spread between the four B field values listed for a given epoch in Table 2 to give a sense of the uncertainty on B: a factor of $\sim$2. As it is likely that the true spectral index is shallower than $\alpha = -0.55$, these B values are likely underestimates.

These magnetic field strengths in V3890 Sgr are comparable with other novae that have been imaged with the VLBA. In V1535 Sco, J. D. Linford et al. (2017) estimate magnetic field strengths of 0.13 G for $K_0 = 40$ and 0.17 G for $K_0 = 100$ about 7.7 d after eruption using a path length of $\sim 10^{13}$ cm, comparable to our day 8.1 estimates in V3890 Sgr assuming $\alpha = -0.7$. In imaging of V1674 Her, M. Williams et al. (in review) estimate the magnetic field on day 20 to be 0.09 G for $K_0 = 40$ and 0.11 G for $K_0 = 100$, very similar to what we find for V3890 Sgr 16 d after eruption (again, assuming $\alpha = -0.7$). RS Oph was also found to have similar magnetic field values, of 0.09 G for $K_0 = 40$ and 0.11 G for $K_0 = 100$ about 21 d after eruption (M. P. Rupen, A. J. Mioduszewski & J. L. Sokoloski 2008).

We also estimate the magnetic field pressure, given by $P_B = \frac{B^2}{8\pi}$. The magnetic field pressures on day 8.1 are 0.003 dyn cm^{-2} for $K_0 = 40$ and $\alpha = -0.55$, and 0.005 dyn cm^{-2} for $K_0 = 100$. On day 16, the magnetic pressure has decreased to 9×10^{-4} dyn cm^{-2} for $K_0 = 40$ and 0.001 dyn cm^{-2} for $K_0 = 100$. By day 51, the magnetic pressure has further declined to 1×10^{-4} dyn cm^{-2}.

These magnetic field determinations will be used to estimate the magnetic pressure fraction (ϵ_B) in Section 5.2.

3.7 Spectral index maps

We combine our 4.87 and 8.37 GHz VLBA images to measure the spectral index α across V3890 Sgr on days 8 and 16 of the eruption. The spectral index maps (SIMs) use images of the nova made in DIFMAP.

Each epoch had identical map and cell sizes. The 4.87 GHz UV data were plotted in RADPL, and the data on the shortest baselines were cut so that the data began at the same minimum UV distance as the corresponding 8.37 GHz data. The 8.37 GHz images were also tapered to have the same beam size as the 4.87 GHz images. This way the UV ranges sampled by the two frequencies are brought into alignment. The fits files were then loaded back into AIPS to make the spectral index maps. Using BLANK the nova was outlined, and regions without significant nova emission were blanked out in both frequencies. Then an image cube was made using FQUB, which was then transposed using TRANS. The SIM was made using SPIXR.

The SIMs are shown in Figs 5 and 6. The more yellow regions correspond to a positive spectral index, brighter at higher frequencies. Contours of the 8.37 GHz image flux [identical to those in panels (a) and (c) of Fig. 1] are added to further show how the spectral index is changing over the source.

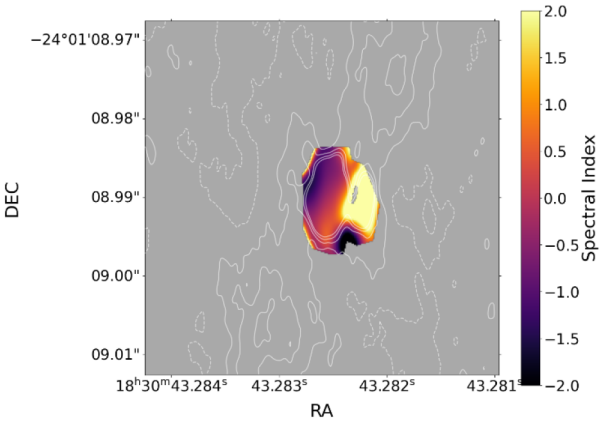


Figure 5. Spectral index map of the September 4 observation, 8.1 d after eruption, using 4.87 and 8.37 GHz. The September 4 8.37 GHz image contours are overlaid on the SIM.

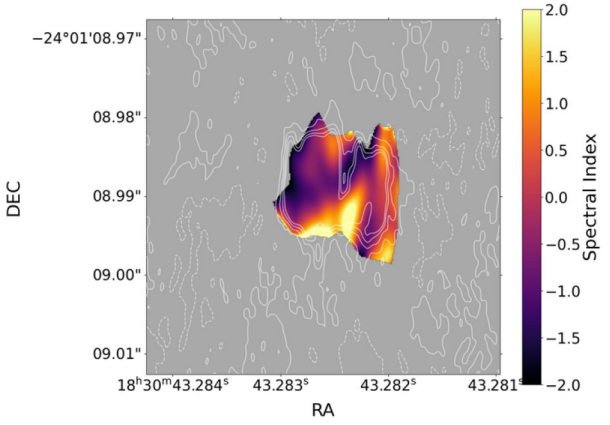


Figure 6. Spectral index map of the September 12 observation, 16 d after eruption, using 4.87 and 8.37 GHz. The September 12 8.37 GHz image contours are overlaid on the SIM.

From the SIM on day 8 (Fig. 5), we see that the spectral index changes over the source, with the eastern region having a spectral index of around -0.5 to 0.5. The western component is more positive with values of $\alpha \approx 2$. This could be explained by the eastern region being optically thin synchrotron emission and the western region still being optically thick, free–free absorbed by intervening CSM (see fig. 2 of U. Munari et al. 2022 for a nice illustration). The hole located just to the west of the image center is due to a small region with negative flux density in the 4.87 GHz image. At this same location, there is significant positive flux from the source in the 8.37 GHz image, $\sim$ 0.0015 Jy. When the two images are overlaid, this results in a non-physical spectral index. The values on the edge of this hole should also be disregarded. Here we have reduced the scale to only allow for a range of $\alpha = -2$ to 2. Due to noise and the differences between the apparent structures in the 4.87 GHz and 8.37 GHz images, the spectral index calculated at the edges of the SIMs should also be disregarded.

In the day 16 SIM, the spectral index in the eastern region becomes more negative, with values ranging from -1 to 0.5. The western region has become flatter, with values ranging from 0.5

Downloaded from academic.oup.com/mnras/article/552/4/stag1851/8842644 by Chalmers tekniska högskola (Chalmers University of Technology) user on 28 October 2026

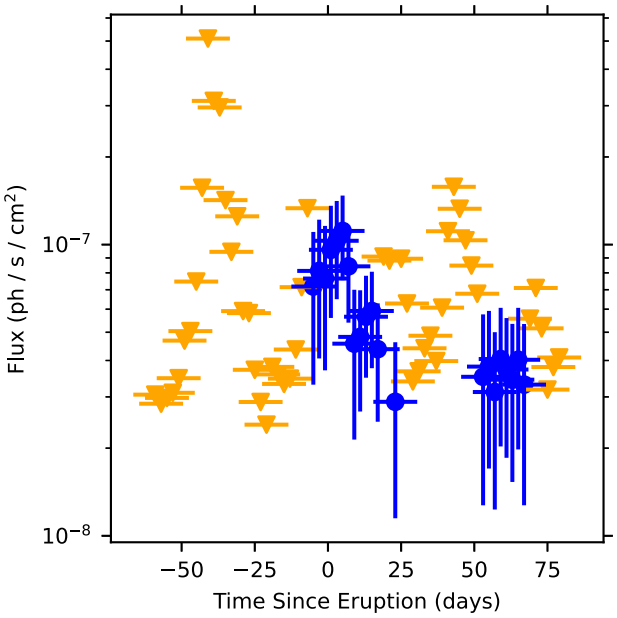


Figure 7. γ-ray light curve for V3890 Sgr obtained using *Fermi*/LAT data with a bin width of 15 d. Blue circular points indicate bins with a test statistic of 4 or greater, corresponding to at least a 2σ detection, while orange upside down triangles show 95 per cent upper limits on the γ-ray flux.

to 2. The negative spectral index seen in the eastern region is as expected for synchrotron emission from shocks originating from ejecta hitting up against strong CSM (J. D. Linford et al. 2017). This is also seen in RS Oph's early radio emission (S. P. S. Eyres et al. 2009).

To attempt to constrain the spectral index of the diffuse emission in the day 48 EVN + e-MERLIN image, we considered the VLA observations published in M. M. Nyamai et al. (2023). High-frequency ($\gtrsim$30 GHz) observations obtained in the VLA's A configuration should be able to resolve this diffuse emission. Unfortunately, while the VLA observations obtained on days 45 and 51 were in A configuration, they were limited to <8 GHz, where resolution is poorer. The VLA observation from day 67 did include higher-frequency data, but were obtained in A-to-D configuration move time, which made extracting a high-resolution image difficult, with limited baselines probing the small angular scales. We conclude that there is no bright flux at 30 GHz resolvable on ∼0.06 arcsec scales, and the VLA data are all consistent with point-like emission. This, along with the fact that the integrated radio spectrum during the second bump maintains a negative spectral index ($\alpha = -0.4$; M. M. Nyamai et al. 2023), leads us to conclude that it is likely that the diffuse emission is brighter at lower frequencies, as expected for synchrotron emission.

4 *FERMI* GEV γ-RAY ANALYSIS

4.1 LAT light curve

V3890 Sgr's >100 MeV γ-ray light curve, as measured by *Fermi*/LAT, is shown in Fig. 7 with time bins that are 15 d wide and sampling every 2 d. The displayed light curve spans 2019 June 29 to November 15, with the maximum flux being 2019 Sep 2 (5 d after start of eruption/optical peak). To convert between photon and energy fluxes, we assume a standard spectral model based on V906 Car (currently the highest S/N γ-ray detection of a nova; E. Aydi et al. 2020), which has been found to be reasonable for most novae (A. Franckowiak et al. 2018). For our energy band, this translates to a conversion factor of 1 photon cm^{-2} s^{-1} = 1.2794×10^{-3} erg cm^{-2} s^{-1} (the same one used by P. Craig et al. 2025). Given the low S/N of the V3890 Sgr detections, the available data are not able to provide better constraints on the γ-ray spectrum of this nova. A maximum flux value of 1.43×10^{-10} erg s^{-1} cm^{-2} with an error of 4.6×10^{-11} erg s^{-1} cm^{-2} were found. A narrower bin, beginning 2 d before the optical peak to ensure that we capture the start of the γ-ray emission, and ending at the observed maximum in the light curve, with free spectral parameters, yields a somewhat larger flux of 2.4×10^{-10} erg s^{-1} cm^{-2}, with a relatively large uncertainty of 1.5×10^{-10} erg s^{-1} cm^{-2}. We take this to be the maximum γ-ray flux during the eruption to estimate the system's γ-ray luminosity.

At a distance of 6.8 kpc, this *Fermi*/LAT flux corresponds to a peak >100 MeV luminosity of $(1.1 \pm 0.6) \times 10^{36}$ erg s^{-1}, or about 1 per cent of the white-dwarf Eddington luminosity. This is more luminous than V745 Sco ($< 5.2 \times 10^{35}$ erg s^{-1} at 8.2 kpc; A. Franckowiak et al. 2018; I. Molina et al. 2024) and V407 Cyg (6.6×10^{35} erg s^{-1} at 3.5 kpc; A. A. Abdo et al. 2010; L. Chomiuk et al. 2021a). V3890 Sgr is significantly less γ-ray luminous than RS Oph at peak (6.7×10^{36} erg s^{-1} at 2.7 kpc; V. A. Acciari et al. 2022; C. C. Cheung et al. 2022). V3890 Sgr's γ-ray luminosity ranks in the top ∼quarter of the classical nova sample of P. Craig et al. (2025), which is focused on novae with main-sequence companions but provides an overview of the state-of-the-art of the population of γ-ray detected novae.

The light curve in Fig. 7 indicates that V3890 Sgr had a peak in the γ-rays around the time of optical maximum, and emitted significantly until 23 d after optical peak. Interestingly, there is a marginal detection (with a detection defined here as a test statistic of at least 4) around day 60, after a series of non-detections. The timing of this γ-ray reappearance is strikingly similar to the timing of the second radio bump (day ∼40–80; Fig. 3 and M. M. Nyamai et al. 2023). Possible explanations for this resurgence of γ-rays and radio emission are considered in Section 5.4.

4.2 LAT test statistic

A plot displaying the test statistic throughout V3890 Sgr's *Fermi*/LAT light curve is shown in Fig. 8. Each point matches a point in the light curve, so the sampling is again a series of bins with a width of 15 d, sampled every 2 d. A horizontal line displays the threshold for a significant detection in the light curve, set to the 2σ level. The highest test statistic recovered in the light curve is 19.0, found on day 5 (also the day with the maximum observed flux), which corresponds to a 4.3σ detection. We note that a larger test statistic can be found with a longer time window, exceeding a 5σ detection (see below). In the tentative secondary peak around day 60, there are a series of several bins with test statistics between 4 and 7, which meet our cut-off for significance in the light curve.

Measuring the duration of the γ-ray emission is tricky in light curves with large, overlapping time windows. Following the methods of A. Franckowiak et al. (2018), we find the test statistic across a range of start and end times. This includes start times at 1 d intervals ranging from 10 d before the optical peak until 10 d after the peak, and end times at 1 d intervals ranging from 1 to 35 d following the optical peak. The exceptions are any start and end time combinations that lead to the start time being the same as or

Downloaded from academic.oup.com/mnras/article/552/4/stag1851/8842644 by Chalmers tekniska högskola (Chalmers University of Technology) user on 28 October 2026

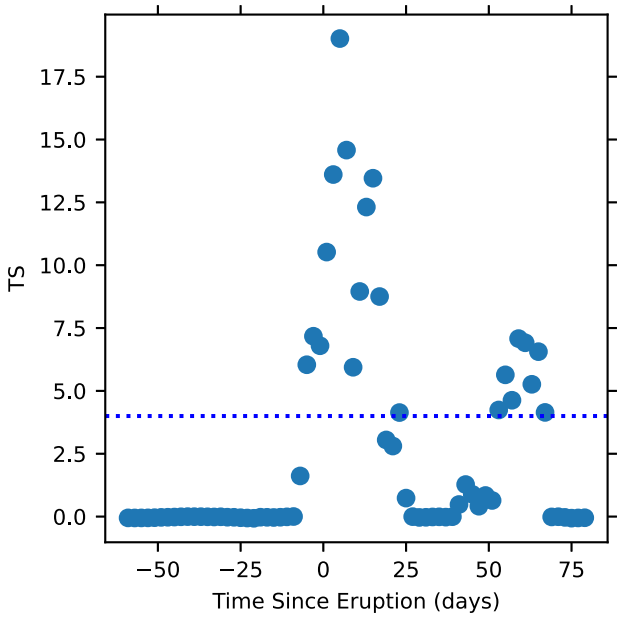


Figure 8. *Fermi*/LAT test statistic on V3890 Sgr as a function of time, with windows of 15 d. Time shown is relative to the optical peak. The horizontal dotted line displays the TS = 4 significance cut-off adopted for the light curve in Fig. 7.The secondary peak in TS seen around day 60 reaches a maximum of 7.1, yielding a secondary marginal detection around this time.

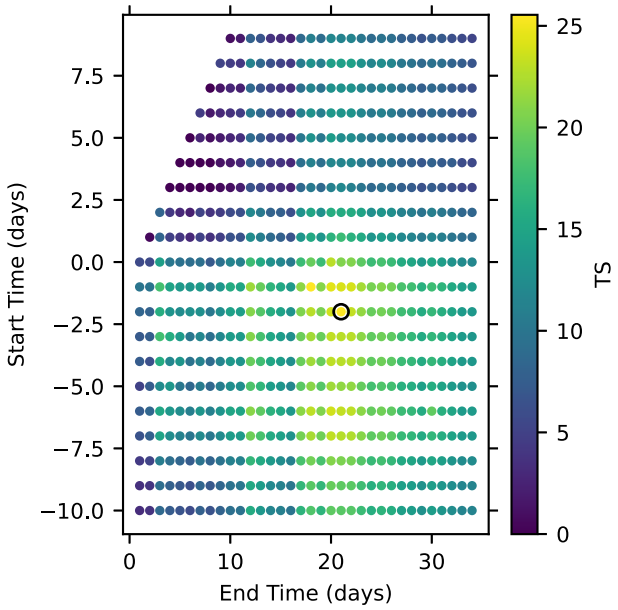


Figure 9. Grid of TS values assuming different windows of data selection for V3890 Sgr. The circled point corresponds to the maximum recovered TS value of 25.5, and a duration of 23 d. The upper left corner is blank because in this region the end times would be before the start times, and therefore there are no data.

after the end time. From this analysis, the maximum TS value is obtained starting 2 d before the optical peak, and continuing until 21 d after the peak, corresponding to a γ-ray duration of 23 d. This solution also corresponds to our maximum TS value of 25.5, a 5σ detection. The assumed spectral model is again a power law with an exponential cut-off (equation 1), but here the power law index and energy cut-off are allowed to vary. The resulting grid of TS values is displayed in Fig. 9.

As the secondary peak around day 60 is only a marginal detection, with the significance peaking at 2.5σ in our light curve, we investigate the rate of false positives at this significance level. The goal is to eliminate the possibility that we are getting false detections due to a poor fit to the background or similar modeling difficulty. In order to make the fairest comparison with our generated light curve, we extend the start time of our light curve to 10 yr before the optical peak for this nova, with increased spacing between bins of 15 d such that adjacent bins do not overlap. Data more than 60 d before the eruption certainly contain no γ-ray emission from the nova eruption itself, so we repeat our analysis at these times to search for false positives. The distribution of test statistics recovered from this data set is shown in Fig. 10. The vertical line displays the same cut-off used in our light curve. Out of 227 independent samples, we find 7 that exceed our TS $>$ 4 significance cut-off, consistent with the 2σ confidence level. Only one of the samples reached TS $\geq$ 7.1, which is the peak TS we measure for the tentative secondary peak. This low false detection rate leads us to have confidence that the secondary γ-ray peak in V3890 Sgr is a valid 2.5σ marginal detection.

By altering the assumed spectrum for the time window 52.5-d 67.5 (centered on day 60) ($\pm$0.5 on the spectral index and a 2–5 GeV cut-off), the flux ranges from $(2-5)\times10^{-8}$ ph s^{-1} cm^{-2}, within our flux uncertainty. Most solutions imply $\sim 2.5\sigma$ significance, but this drops once the spectral index exceeds $\gamma_1 \sim 2.3$.

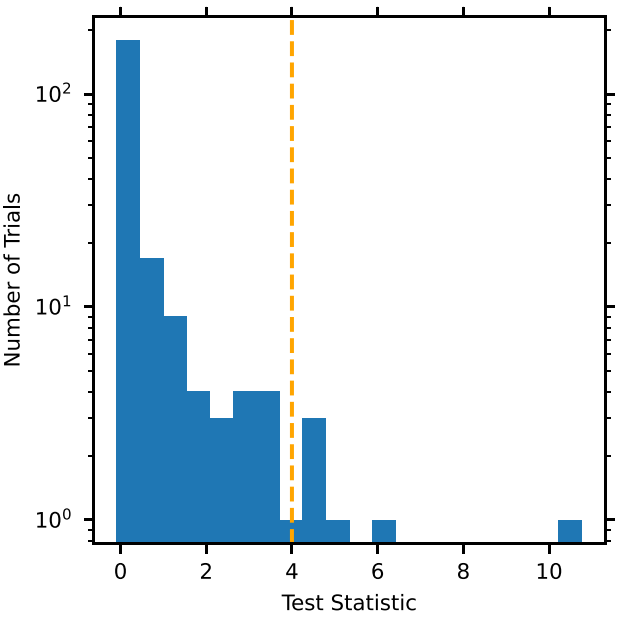


Figure 10. Histogram showing the obtained *Fermi*/LAT test statistic values from background-sampled regions. The vertical orange line displays the cut-off for a significant detection (TS $>$ 4). Only 2.6 per cent of our background samples would meet this criterion, and one out of 227 trials matches or exceeds the observed test statistic value in the secondary peak (TS $>$ 7.1).

Downloaded from academic.oup.com/mnras/article/552/4/stag1851/8842644 by Chalmers tekniska högskola (Chalmers University of Technology) user on 28 October 2026

5 MODELLING THE SHOCK IN V3890 SGR

5.1 Density of the shocked gas

The density of the gas being shocked, ρ, is a key parameter in determining shock signatures. In V3890 Sgr, ρ is the density of the pre-existing CSM, expelled from the red giant as a wind. Here, we assume a spherical wind of constant mass-loss rate $\dot{M}_{\rm w}$ and velocity $v_{\rm w}$, which yields a CSM density profile of

$$\rho = \frac{\dot{M}_{\rm w}}{4\pi v_{\rm w} r^2}. \quad (4)$$

While the CSM in V3890 Sgr is likely more complex than a simple spherical wind, our VLBI images show that, at least for the first 32 d, the radio-emitting shock is likely to be interacting with the lower-density spherical component (as opposed to the EDE). This shock component, with relatively low absorption (as opposed to the shocks in the orbital plane, which are likely dominating the γ-rays; Section 5.3), is also most likely to produce the X-rays detectable by *Swift*/XRT.

We therefore estimate ρ from the hard X-ray emission observed by *Swift*/XRT (K. L. Page et al. 2020); APEC normalization factors and temperatures from these observations are listed in Table 3. While the X-ray plasma temperatures listed in Table 3 are rather low, similarly modest X-ray temperatures have been measured in other symbiotic recurrent novae at 1 week after optical peak (e.g. RS Oph and V745 Sco; L. Delgado & M. Hernanz 2019; M. Orio et al. 2023). It is possible that the hot X-ray plasma is mixing with cooler gas from behind the shock, reducing the temperature.

The APEC normalization factor constrains the number density of electrons and ions as

$$\mathrm{Norm} = \frac{10^{-14}}{4\pi D^2} \int n_{\rm e} n_{\rm H} {\rm d}V. \quad (5)$$

We solve for n_H assuming that $n_{\rm e} = n_{\rm H}$, $D = 6.8$ kpc, and V is the volume of the hot shocked region. We assume the hot APEC component is filling the volume between the forward shock and the contact discontinuity, take the radius of the forward shock from our VLBA images, and estimate the radius of the contact discontinuity ($R_{\rm CD}$) from the formalism described in X. Tang & R. A. Chevalier (2017) and M. M. Nyamai et al. (2023): $R_{\rm CD} \approx 0.35\,R_{\rm FS}$ over the time-scale of our VLBA observations. The resulting densities of the hot shocked gas are listed in Table 3. For estimating an uncertainty on this density, we propagate through the APEC uncertainty and also assume a 10 per cent uncertainty on our radius measurements, which reflect difficult-to-quantify uncertainties in the source morphology. A 10 per cent uncertainty on radius translates to a 30 per cent uncertainty on volume, which dominates the uncertainties in most epochs.

These $n_{\rm H}$ estimates can be used to estimate ρ, the density of the gas being shocked, assuming a compression ratio of 4 as expected for a strong shock. We estimate the mass-loss rate into the spherical component of the CSM, $\dot{M}_{\rm w}$, from equation (4), assuming $v_{\rm w} = 10$ km s^{-1} as expected for a red giant, the radii from our VLBA images, and $D = 6.8$ kpc. These $\dot{M}_{\rm w}$ estimates are also given in Table 3, along with uncertainties propagated through from APEC uncertainties.

We find that $\dot{M}_{\rm w} \approx 2 \times 10^{-7}$ M$_\odot$ yr^{-1} in V3890 Sgr, consistently across our four imaging epochs as expected if the CSM truly is distributed as a wind. There is some indication that the $\dot{M}_{\rm w}$ derived from the two later epochs is lower than in the first two epochs, but these variations are within the uncertainties borne of uncertain APEC normalization and shock volume. We also note that this estimate is model-dependent, depending on several assumptions like the metallicity and ionization state of the gas (we assume $n_e = n_{\rm H}$).

To sanity check this estimate of $\dot{M}_{\rm w}$, we searched for radio observations of V3890 Sgr in quiescence, when free–free thermal emission is expected to dominate, driven by the CSM ionized by the accreting white dwarf (E. R. Seaquist & A. R. Taylor 1990). While there are no targeted observations in the VLA archive, we obtained limits on the radio flux from the VLA Sky Survey (VLASS; M. Lacy et al. 2020). VLASS Epoch 1.1 observed V3890 Sgr on 2018 Feb 17, and reveals a low-significance peak (2.9σ) near the position of V3890 Sgr. We are not confident that this is a detection, and therefore take a 3σ upper limit of <0.59 mJy at 3.0 GHz. Using equation (2) of E. R. Seaquist & A. R. Taylor (1990) and assuming $\alpha = 0.6$ in quiescence (A. E. Wright & M. J. Barlow 1975), we estimate an upper limit on $\dot{M}_{\rm w}$ of $< 5 \times 10^{-7}$ M$_\odot$ yr^{-1}, consistent with our X-ray estimates.

$\dot{M}_{\rm w} = 2 \times 10^{-7}$ M$_\odot$ yr^{-1} is typical for a symbiotic star, whose $\dot{M}_{\rm w}$ span $10^{-8} - 10^{-5}$ M$_\odot$ yr^{-1} (E. R. Seaquist & A. R. Taylor 1990; E. R. Seaquist, M. Krogulec & A. R. Taylor 1993). However, it is significantly higher than other symbiotic recurrent novae, like V745 Sco ($\dot{M}_{\rm w} = 2 \times 10^{-8}$ M$_\odot$ yr^{-1}; S. Orlando et al. 2017; I. Molina et al. 2024), and T CrB ($\dot{M}_{\rm w} = 2 \times 10^{-9}$ M$_\odot$ yr^{-1}; S. Orlando et al. 2025). The symbiotic recurrent nova RS Oph also has a lower $\dot{M}_{\rm w} \approx 6 \times 10^{-8}$ M$_\odot$ yr^{-1} in the spherical CSM component (S. Orlando et al. 2025), but $\dot{M}_{\rm EDE} \approx 2 \times 10^{-7}$ M$_\odot$ yr^{-1} in the EDE (for comparable $v_{\rm w} = 10$ km s^{-1}; R. Lico et al. 2024), implying CSM that is more strongly confined to the orbital plane than in V3890 Sgr.

Our estimate of $\dot{M}_{\rm w}$ is also significantly higher than the mass-loss rate estimated from modelling V3890 Sgr's radio light curve in M. M. Nyamai et al. (2023): $\dot{M}_{\rm w} \approx 10^{-8}$ M$_\odot$ yr^{-1}, but we note their estimate depends crucially on the poorly known efficiencies of amplifying magnetic fields and accelerating relativistic electrons, and that it is possible to get good fits to the radio light curve with $\dot{M}_{\rm w} = 2 \times 10^{-7}$ M$_\odot$ yr^{-1}. The relatively dense environment of V3890 Sgr, and the relatively spherical distribution of the CSM (as opposed to confinement in an EDE) likely explains why its radio flux is so bright and radio images reach good S/N, even at a relatively large distance of 6.8 kpc. Its 5 GHz spectral radio luminosity at $d = 6.8$ kpc is 2.9×10^{21} erg s^{-1} Hz^{-1}, a factor of $\sim$ 4-5 greater than RS Oph (R. M. Hjellming et al. 1986; S. P. S. Eyres et al. 2009) and V745 Sco (I. Molina et al. 2024).

5.2 Efficiency of magnetic-field amplification and Lepton acceleration

We can use the magnetic field estimates from Section 3.6 to constrain the efficiency with which the shock accelerates leptons (ϵ_e) and the fraction of the post-shock pressure in magnetic fields ($\epsilon_{\rm B}$). We remind the reader that B was estimated assuming equipartition with relativistic electrons, such that implicitly $\epsilon_{\rm B} = \epsilon_{\rm e}$, where $\epsilon_{\rm e}$ is the fraction of the post-shock pressure in relativistic electrons, $\epsilon_{\rm B}$ is defined such that $\frac{B^2}{8\pi} = \epsilon_{\rm B}\,\rho\,v_{\rm s}^2$, and ρ is the density of gas being shocked. These ϵ factors are commonly used in modelling radio emission from diverse astrophysical transients (e.g. R. A. Chevalier 1982; P. Chandra & D. A. Frail 2012; M. F. Bietenholz et al. 2021; R. Margutti & R. Chornock 2021). Table 2 lists B and $v_{\rm s}$ estimates from our VLBI images, and we estimate ρ

Downloaded from academic.oup.com/mnras/article/552/4/stag1851/8842644 by Chalmers tekniska högskola (Chalmers University of Technology) user on 28 October 2026

Table 3. Properties derived from X-ray spectra of V3890 Sgr.

Day	kT_{hot} (keV)	$Norm_{hot}$ (cm^{-5})	kT_{cool} (keV)	$Norm_{cool}$ (cm^{-5})	n_H(hot) (10^6 cm^{-3})	$\dot{M}_w$ (10^{-7} $M_\odot$ yr^{-1})
7.7	$2.8^{+1.1}_{-0.7}$	$0.064^{+0.014}_{-0.010}$	–	–	11.1 ± 2.0	2.2 ± 0.4
15.5	$2.1^{+0.3}_{-0.2}$	$0.041^{+0.003}_{-0.005}$	$0.76^{+0.20}_{-0.15}$	$0.017^{+0.006}_{-0.006}$	4.2 ± 0.7	2.3 ± 0.3
31.9	$1.5^{+5.9}_{-0.3}$	$0.017^{+0.006}_{-0.012}$	$0.62^{+0.37}_{-0.29}$	$0.011^{+0.007}_{-0.005}$	$1.1^{+0.3}_{-0.5}$	$1.9^{+0.4}_{-0.7}$
51.4	< 0.9	$0.008^{+0.001}_{-0.001}$	–	–	0.49 ± 0.08	1.6 ± 0.3

from the spherical CSM component $\dot{M}_w$ estimated in the previous subsection. The resulting values of ϵ_B are listed in Table 2.

Our estimates of ϵ_B and ϵ_e range from 5×10^{-4} to 7×10^{-3}, depending on the epoch and the assumed values of K_0 and α. There is a variation of a factor of ∼4 between the ϵ_B values listed in Table 2 for a given epoch, which demonstrates the level of uncertainty on ϵ_B borne of K_0 and α. Moreover, uncertainty carried over from the density calculations implies errors of ∼17 per cent on days 8.1, 16.0, and 51.0, and $^{+23}_{-39}$ per cent on day 32.0, which is dwarfed by uncertainty in treating α. We again remind the reader that the true α is likely to be shallower than −0.55, which would imply stronger B fields and higher ϵ_B. There is a need for a framework that treats synchrotron sources with $\alpha < -0.5$ properly (as these appear to occur frequently amongst novae), but this is outside the scope of the paper as it requires significant work and is dependent on assumptions about the high-energy end of the relativistic lepton spectrum.

The equipartition parameters estimated here for V3890 Sgr are smaller than what is often taken or inferred in studies of supernovae and γ-ray bursts (R. A. Chevalier & C. Fransson 2006; P. Chandra & D. A. Frail 2012; L. Chomiuk et al. 2016), which might be the result of the relatively low shock speeds in novae. For example, if the magnetic field is amplified via the non-resonant streaming instability (A. R. Bell 2004), then ϵ_B scales as $v_s\epsilon_p$, where ϵ_p is the proton acceleration efficiency (see e.g. R. Diesing et al. 2023, for a detailed implementation). Moreover, estimates of ϵ_e in supernova remnants, which have shock velocities similar to those seen in novae, find similarly low efficiencies (G. Morlino & D. Caprioli 2012; S. K. Sarbadhicary et al. 2017).

There is some surprising indication that the efficiencies seem to increase between day 8 and 32 in V3890 Sgr, counter to expectations for a decelerating shock. While the ϵ_B variations between epochs are technically larger than our formal uncertainty (assuming a fixed K_0/α), we are skeptical that this should be interpreted as real variations in ϵ_B, given significant uncertainty in both the input parameters and modelling. We prefer the $\alpha = -0.55$ ϵ_B values, which lead us to conclude $\epsilon_B =$ few $\times 10^{-3}$, but note ϵ_B should be fully self-consistently modelled in the future, accounting for the radio spectral index which is likely $\alpha < -0.5$.

5.3 Lessons from simultaneous modelling of radio and γ-ray emission

V3890 Sgr achieved a peak γ-ray luminosity of $L_\gamma \approx 1.3 \times 10^{36}$ erg s^{-1} around the time of optical peak, assuming a distance of 6.8 kpc. The maximum possible L_γ is the calorimetric limit, in which accelerated protons lose all of their energy in proton–proton collisions such that $L_\gamma = \kappa L_p$, where $\kappa \approx 0.1$ is the fraction of the proton energy that goes into γ-rays, and L_p is the cosmic ray (proton) luminosity (e.g. B. D. Metzger et al. 2015). Taking $L_p = \epsilon_p L_s \approx \epsilon_p M_{ej} v_s^2 / t_{age}$, where L_s is the shock luminosity, M_{ej} is the nova ejecta mass, and t_{age} is the nova age, we approximate:

$$L_\gamma \approx 2.3 \times 10^{35} \text{ erg s}^{-1} \times \left(\frac{\epsilon_p}{10^{-2}}\right)\left(\frac{M_{ej}}{10^{-6} M_\odot}\right)\left(\frac{v_s}{1000 \text{ km s}^{-1}}\right)^2\left(\frac{t_{age}}{\text{day}}\right)^{-1}. \quad (6)$$

Thus, for $M_{ej} \approx 10^{-6} M_\odot$ (M. M. Nyamai et al. 2023) and $v_s \approx$ 5000 km s^{-1}, we obtain the observed $L_\gamma \approx 1.3 \times 10^{36}$ erg s^{-1} at $t_{age} = 4$ d.

Of course, even higher values of L_γ may be achievable at earlier times (the peak date of the γ-rays is uncertain) or with less conservative assumptions about the ejecta mass and acceleration efficiency. However, the fact remains that, to produce sufficient γ-ray flux, the density of the shocked gas must be very large, such that the pion production time-scale, τ_{pp}, is comparable to (or less than) t_{age}. Taking $\tau_{pp} \approx 260$ d $\times$ (10^8 cm^{-3}/n_H) (R. Diesing et al. 2023), we obtain a density, $n_H \gtrsim 6.5 \times 10^9$ cm^{-3}, at $t_{age} = 5$ d. Not only is this density much larger than that inferred in Section 5.1, it is almost certainly opaque to radio due to the large free–free optical depth. Note that a comparable density must be maintained until at least $t_{age} \gtrsim 20$ d – well after the radio detection – since the γ-ray emission remains bright until that time.

In short, consistent with previous analysis in the context of classical novae (e.g. A. Vlasov, I. Vurm & B. D. Metzger 2016), the γ-ray emission cannot arise from the same region as the radio. The most natural explanation is CSM characterized by an EDE. In this picture, a spherical outflow interacts with an aspherical environment: the interaction between the outflow and the dense equatorial medium produces a large γ-ray luminosity (but free–free absorption occludes any radio emission), while the interaction between the outflow and the lower-density red giant wind in the polar regions is responsible for the radio observations. This picture is consistent with the bipolar structure observed with VLBA at intermediate times (16 d $\lesssim t_{age} \lesssim$ 32 d).

This picture is also supported by a comparison of radio and γ-ray luminosities of novae with evolved companions. While the peak 5 GHz radio luminosity scales with the density of the spherical wind component (Section 5.1), the γ-ray luminosity does not. V407 Cyg had denser spherical CSM than V3890 Sgr ($\dot{M}_w = 10^{-6}$ $M_\odot$ yr^{-1}; L. Chomiuk et al. 2012) but less luminous γ-rays (Section 4.1), while RS Oph is characterized by lower $\dot{M}_w$ and yet has more luminous γ-rays. We therefore predict that, of these three novae, RS Oph had the densest EDE and V407 Cyg had the least dense. This is consistent with expectations for mass transfer by wind Roche lobe overflow, where a larger fraction of the CSM is expected to be confined in the EDE for symbiotic binaries with smaller separations (S. Mohamed & P. Podsiadlowski 2012).

Downloaded from academic.oup.com/mnras/article/552/4/stag1851/8842644 by Chalmers tekniska högskola (Chalmers University of Technology) user on 28 October 2026

5.4 Origin of the late-time diffuse radio emission

The late-time radio excess observed in V3890 Sgr around $t \simeq$ 45–60 d cannot be explained by direct emission from the forward shock traced by our VLBI images. At these epochs, the angular extent of the diffuse radio emission detected by the EVN + e-MERLIN (~ 0.1 arcsec, corresponding to physical scales $\sim 10^{16}$ cm at $d = 6.8$ kpc) is far larger than can be reached by ballistic nova ejecta expanding at the observed velocities ($\lesssim$ 5000 km s^{-1}; Section 3.3). This disfavors an origin in freshly shocked ejecta or a simple density enhancement encountered by the forward shock.

Instead, we propose that the late-time radio emission arises from a *synchrotron halo*: non-thermal particles escaping from the γ-ray–producing shock and diffusing upstream, to interact with pre-existing CSM at a relatively large radius. In this picture, we focus on the shock in the equatorial region which, due to the large inferred post-shock density, is likely radiative; Section 5.3. Relativistic electrons and positrons – produced in proton–proton interactions within the dense, radiative, and relatively unmagnetized shell – leak out of the acceleration region, propagate into the unshocked CSM, and radiate synchrotron emission over much larger spatial scales. In Appendix A, we present a simple analytic model for this synchrotron halo, demonstrating that the order-of-magnitude of the observed radio luminosity, spectral properties, and spatial extent can be reproduced with physically reasonable parameters.

In this framework, the forward shock continues to accelerate hadrons and leptons at late times, particularly as indicated by the γ-ray re-brightening, but a fraction of the non-thermal particle population escapes upstream. Such escape is expected once the shock weakens and the surrounding medium becomes less confining, particularly for high-energy protons and secondary leptons. Moreover, if the observed γ-rays are produced predominantly through hadronic interactions, then charged pion decay naturally injects relativistic electron–positron pairs with Lorentz factors $\gamma \sim 10^2$–10^4, comparable to those required to produce GHz synchrotron emission in magnetic fields of order 10^{-4}–10^{-2} G.

As these particles stream or diffuse into the unshocked red giant wind, they encounter pre-existing magnetic fields carried by the wind itself. For plausible red giant surface fields of order ∼G and flux-freezing in the outflow, the magnetic field strength at radii $\sim 10^{15}$–10^{16} cm is expected to be $B \sim 10^{-3}$–10^{-2} G, comparable to or slightly below the magnetic fields we infer in the shocked region at earlier times (Section 3.6). Additional amplification may occur if escaping non-thermal ions drive plasma instabilities in the upstream medium (e.g. A. R. Bell 2004) or if the latter gas was shocked and compressed by a previous recurrent nova eruption (Section A3).

Because the synchrotron cooling time of relativistic leptons in such fields is much longer than both the wind expansion time and the particle transport time, the emitting particles are firmly in the slow-cooling regime (Section A4). As a result, the radio luminosity reflects the cumulative injection and transport of non-thermal particles rather than local radiative losses. This naturally produces a low-surface-brightness, extended radio halo whose characteristic size is set by particle propagation rather than by ejecta dynamics.

A natural question raised by this scenario is why the diffuse radio halo (and corresponding bump in the radio light curve) appears contemporaneously with the second γ-ray peak, rather than being dominated by particles accelerated during the earlier, more luminous γ-ray phase near optical maximum. Those early shocks undoubtedly produced large numbers of non-thermal particles, which in principle could also escape upstream and propagate to large radii.

If pairs were only produced during the first γ-ray peak, when the shock was still compact, then the delayed rise-time of the radio halo could in principle be attributed to the finite time required for the pairs to diffuse upstream into the red giant wind. However, it would then be a coincidence that the radio rebrightening occurred roughly contemporaneous with the second γ-ray peak. If the latter indicates ongoing shock interaction continuing to larger radii, the pairs released from this later shock phase may dominate the observed emission. In particular, particles injected at early times escape at relatively small radii, $r_0 \ll 10^{15}$ cm, and subsequently suffer substantial adiabatic energy losses as they propagate outward through the red giant wind. By the time such particles reach radii $\sim 10^{16}$ cm, their Lorentz factors have been reduced by factors of $\sim r_0/r$, shifting their synchrotron emission to frequencies well below the GHz band and rendering their contribution to the observed radio halo negligible.

The second γ-ray peak could mark the interaction of the nova ejecta with a denser circumstellar structure at $r \sim 10^{15}$ cm, such as a secondary density enhancement in the red giant wind or EDE inferred from the radio light curve. Shocks formed at these larger radii inject non-thermal particles with a much larger effective escape radius r_0. Because the subsequent adiabatic degradation from $r_0 \sim 10^{15}$ cm to $r \sim 10^{16}$ cm is modest, these particles retain sufficiently high Lorentz factors to radiate efficiently at GHz frequencies. As a result, the late-time shocks dominate the observable synchrotron halo, even if the total non-thermal energy injected at earlier times was larger.

6 CONCLUSION

We present VLBI radio imaging and *Fermi*/LAT GeV γ-ray monitoring of the 2019 eruption of the symbiotic recurrent nova V3890 Sgr. VLBI imaging spans 8–51 d following eruption, concurrent with the detected γ-rays. We conclude:

(i) The VLBI images start out asymmetric on day 8, with the eastern component brighter than the western component. However, the western component brightens with time, and by day 32, the radio-emitting shell is quite circularly symmetric. We explain this evolution as bipolar expansion, with a density enhancement in the orbital plane oriented north–south and the western component absorbed by the EDE at early times (as in RS Oph; U. Munari et al. 2022; R. Lico et al. 2024). In the EVN + e-MERLIN image from day 48, the shell appears brighter in the north–south direction, implying that at late times the shocks interacting with the denser EDE become visible at radio frequencies.

(ii) We measure the expansion of the radio-emitting shell and compare it with radial velocities from optical spectroscopy. We thereby estimate an expansion parallax distance to V3890 Sgr of 6.8 kpc (Section 3.3). The radio images suggest significant deceleration of the shock between the first imaging epoch on day 8 and later epochs, from ∼6000 km s^{-1} to 3100 km s^{-1}.

(iii) By comparing the flux recovered from our VLBI imaging with integrated flux from the VLA (M. M. Nyamai et al. 2023), we conclude that the VLBA is detecting most (>80 per cent) of the radio flux on days 8–32, confirming that the radio emission

Downloaded from academic.oup.com/mnras/article/552/4/stag1851/8842644 by Chalmers tekniska högskola (Chalmers University of Technology) user on 28 October 2026

is characterized by high brightness temperatures only achievable with non-thermal emission ($> 10^7$ K).

(iv) On day 51, the VLBA resolves out $\sim$ a third of the integrated flux, but the EVN + e-MERLIN recovers this missing flux and finds it is distributed in a diffuse halo $\gtrsim 10^{16}$ cm across with peak $T_B \approx 10^5$ K. The appearance of this radio halo is coincident with a second peak in the VLA radio light curve (Fig. 3) and in the γ-ray light curve (Fig. 7). The radio spectrum of this second peak and the brightness temperature of the diffuse flux significantly in excess of 10^4 K lead us to conclude that this halo is powered by synchrotron emission.

(v) We find the >100 MeV γ-rays peak at a flux of $(1.9 \pm 1.2) \times 10^{-7}$ phot s^{-1} cm^{-2} ($L_\gamma = 1.3 \times 10^{36}$ erg s^{-1} at 6.8 kpc) around the time of optical maximum. The γ-rays remain detectable for 23 d, and then reappear at 2.5σ significance around day 60, contemporaneous with the second peak in the radio light curve (Section 4.1).

(vi) By modelling the simultaneous γ-ray and radio emission from V3890 Sgr, we conclude that radio emission and γ-rays must be originating from different portions of the shock: the high γ-ray luminosity requires a very dense medium for efficient pion production, while such a dense medium would free–free absorb radio emission. It is likely that the radio-emitting shock marks the ejecta's interaction with a spherical wind-like component of the CSM, while the γ-rays originate from interaction with an overdensity of CSM in the orbital plane (Section 5.3).

(vii) We estimate the density of the CSM from X-ray observations of the hot shocked gas (K. L. Page et al. 2020), finding that the CSM can be parameterized as a spherical wind with $\dot{M}_w = 2 \times 10^{-7}$ M$_\odot$ yr^{-1} (assuming $v_w = 10$ km s^{-1}), plus denser material in the orbital plane. This is significantly denser than the CSM estimated in other symbiotic recurrent novae (Section 5.1).

(viii) By combining our velocity, magnetic field, and CSM density measurements, we can estimate the fraction of the post-shock pressure in magnetic fields, and find $\epsilon_B \approx$ few $\times 10^{-3}$ (Section 5.2). We assume equipartition with relativistic electrons, so similar values of ϵ_e are implied.

(ix) The $\sim 10^{16}$ cm synchrotron halo and late-time radio bump **may** be explained by relativistic leptons that escape the shocked shell (most of secondary origin) and interact with CSM upstream of the shock (Section 5.4).

ACKNOWLEDGEMENTS

Support for this work was provided by the National Science Foundation through the Grote Reber Fellowship Program administered by Associated Universities, Inc./National Radio Astronomy Observatory. Nova science at Michigan State is supported by National Science Foundation grant AST-2107070 and National Aeronautics and Space Administration grants 80NSSC23K0497, 80NSSC25K7334, and 80NSSC23K1247. RD and BDM were supported in part by National Aeronautics and Space Administration (grants 80NSSC22K0807, 80NSSC24K0408), the Simons Foundation (grant PG013158), and Columbia University through the Research Stabilization Fund. The Flatiron Institute is supported by the Simons Foundation. KLP acknowledges support from the UK Space Agency. JLS acknowledges support from National Aeronautics and Space Administration grants 80NSSC25K0622 and 80NSSC25K7082.

The National Radio Astronomy Observatory and Green Bank Observatory are facilities of the U.S. National Science Foundation operated under cooperative agreement by Associated Universities, Inc. This work made use of the Swinburne University of Technology software correlator (A. T. Deller et al. 2011), developed as part of the Australian Major National Research Facilities Programme and operated under license. The European VLBI Network is a joint facility of independent European, African, Asian, and North American radio astronomy institutes. Scientific results from data presented in this publication are derived from the following European VLBI Network project code(s): RY008. e-MERLIN, *enhanced* Multi Element Remotely Linked Interferometer Network, is a National Facility operated by the University of Manchester at Jodrell Bank Observatory on behalf of STFC. The research leading to these results has received funding from the European Commission Horizon 2020 Research and Innovation Programme under grant agreement No. 730562 (RadioNet). e-VLBI research infrastructure in Europe is supported by theEuropean Union's Seventh Framework Programme (FP7/2007-2013) under grant agreement number RI-261525 NEXPReS.

DATA AVAILABILITY

The radio images presented in this paper are available for download in fits format from Zenodo.

REFERENCES

Abdo A. A. et al., 2010, Science, 329, 817
Abdollahi S. et al., 2022, ApJS, 260, 53
Acciari V. A. et al., 2022, Nat. Astron., 6, 689
Ackermann M. et al., 2014, Science, 345, 554
Anupama G. C., Sethi S., 1994, MNRAS, 269, 105
Anupama G. C. et al., 2013, A&A, 559, A121
Aydi E. et al., 2020, Nat. Astron., 4, 776
Basu J., Anupama G. C., Ness J.-U., Singh K. P., Barway S., Chamoli S., 2025, ApJ, 994, 229
Beck R., Krause M., 2005, Astron. Nachr., 326, 414
Bell A. R., 2004, MNRAS, 353, 550
Bietenholz M. F., Bartel N., Argo M., Dua R., Ryder S., Soderberg A., 2021, ApJ, 908, 75
Bode M. F., Evans A., 2008, Classical Novae. Cambridge Univ. Press, Cambridge, p. 16
Booth R. A., Mohamed S., Podsiadlowski P., 2014, in Ray A., McCray R. A. eds, IAU Symp. Vol. 296, Supernova Environmental Impacts. Cambridge Univ. Press, Cambridge, p. 382
Buckley D. A. H., Wargau W. F., Soltynski M. G., Shao C.-Y., Hazen M. L., 1990, IAU Circ., 5019, 1
Buson S., Jean P., Cheung C. C., 2019, Astron. Telegram, 13114, 1
Chandra P., Frail D. A., 2012, ApJ, 746, 156
Chen H.-L., Woods T. E., Yungelson L. R., Gilfanov M., Han Z., 2016, MNRAS, 458, 2916
Cheung C. C. et al., 2022, ApJ, 935, 44
Chevalier R. A., 1982, ApJ, 259, 302
Chevalier R. A., Fransson C., 2006, ApJ, 651, 381
Chomiuk L. et al., 2012, ApJ, 761, 173
Chomiuk L. et al., 2014, Nature, 514, 339
Chomiuk L. et al., 2016, ApJ, 821, 119
Chomiuk L., Metzger B. D., Shen K. J., 2021a, ARA&A, 59, 391
Chomiuk L. et al., 2021b, ApJS, 257, 49
Craig P. et al., 2025, MNRAS, 538, 2339
Darnley M. J., 2021, in The Golden Age of Cataclysmic Variables and Related Objects V, Volume 368, p. 44
Darnley M. J., Williams S. C., Bode M. F., Henze M., Ness J.-U., Shafter A. W., Hornoch K., Votruba V., 2014, A&A, 563, L9
Delgado L., Hernanz M., 2019, MNRAS, 490, 3691
Deller A. T. et al., 2011, PASP, 123, 275

Downloaded from academic.oup.com/mnras/article/552/4/stag1851/8842644 by Chalmers tekniska högskola (Chalmers University of Technology) user on 28 October 2026

Diesing R., Metzger B. D., Aydi E., Chomiuk L., Vurm I., Gupta S., Caprioli D., 2023, ApJ, 947, 70
Evans A., Geballe T. R., Woodward C. E., Banerjee D. P. K., Gehrz R. D., Starrfield S., Shahbandeh M., 2022, MNRAS, 517, 6077
Eyres S. P. S. et al., 2009, MNRAS, 395, 1533
Finzell T. et al., 2018, ApJ, 852, 108
Franckowiak A., Jean P., Wood M., Cheung C. C., Buson S., 2018, A&A, 609, A120
Frostig D. et al., 2026, Astron. Tel., 17801, 1
Gaia Collaboration et al. 2016, A&A, 595, A1
Gaia Collaboration et al. 2023, A&A, 674, A1
Gallagher J. S., Starrfield S., 1978, ARA&A, 16, 171
Gehrz R. D., Truran J. W., Williams R. E., Starrfield S., 1998, PASP, 110, 3
Giroletti M. et al., 2020, A&A, 638, A130
Gordon A. C., Aydi E., Page K. L., Li K.-L., Chomiuk L., Sokolovsky K. V., Mukai K., Seitz J., 2021, ApJ, 910, 134
Green D. A., 2019, JA&A, 40, 36
Greisen E. W., 2003, AIPS, the VLA, and the VLBA. Springer, Dordrecht, p. 109
Harrison T. E., Johnson J. J., Spyromilio J., 1993, AJ, 105, 320
Healy-Kalesh M. W., Darnley M. J., Shara M. M., Lanzetta K. M., Garland J. T., Gromoll S., 2024, MNRAS, 529, 236
Hjellming R. M., van Gorkom J. H., Taylor A. R., Sequist E. R., Padin S., Davis R. J., Bode M. F., 1986, ApJ, 305, L71
Kaminsky B. et al., 2022, MNRAS, 517, 6064
Kemp A. J., Karakas A. I., Casey A. R., Izzard R. G., Ruiter A. J., Agrawal P., Broekgaarden F. S., Temmink K. D., 2021, MNRAS, 504, 6117
Kenyon S. J., 1986, The Symbiotic Stars. Cambridge Univ. Press, Cambridge
Lacy M. et al., 2020, PASP, 132, 035001
Lico R. et al., 2024, A&A, 692, A107
Linford J. D. et al., 2017, ApJ, 842, 73
Margutti R., Chornock R., 2021, ARA&A, 59, 155
Metzger B. D., Finzell T., Vurm I., Hascoët R., Beloborodov A. M., Chomiuk L., 2015, MNRAS, 450, 2739
Metzger B. D., Lancaster L., Diesing R., 2025, ApJ, 988, 211
Mikolajewska J., 2010, preprint (arXiv:1011.5657)
Mikołajewska J., Iłkiewicz K., Gałan C., Monard B., Otulakowska-Hypka M., Shara M. M., Udalski A., 2021, MNRAS, 504, 2122
Miller L. T. P., 1991, JAAVSO, 20, 182
Mitrani S., Behar E., Orio M., Worley J., 2025, ApJ, 989, 166
Mohamed S., Podsiadlowski P., 2012, Balt. Astron., 21, 88
Mohamed S., Booth R., Podsiadlowski P., 2013, in Di Stefano R., Orio M., Moe M. eds, IAU Symposium Vol. 281, Binary Paths to Type Ia Supernovae Explosions. Cambridge Univ. Press, Cambridge, p. 195
Molina I. et al., 2024, MNRAS, 534, 1227
Morlino G., Caprioli D., 2012, A&A, 538, A81
Munari U., Giroletti M., Marcote B., O'Brien T. J., Veres P., Yang J., Williams D. R. A., Woudt P., 2022, A&A, 666, L6
Nelson T., Donato D., Mukai K., Sokoloski J., Chomiuk L., 2012, ApJ, 748, 43
Nelson T. et al., 2019, ApJ, 872, 86
Ness J. U. et al., 2022, A&A, 658, A169
Nyamai M. M., Woudt P. A., Ribeiro V. A. R. M., Chomiuk L., 2019, Astron. Telegram, 13089, 1
Nyamai M. M., Linford J. D., Allison J. R., Chomiuk L., Woudt P. A., Ribeiro V. A. R. M., Sarbadhicary S. K., 2023, MNRAS, 523, 1661
Orio M. et al., 2020, ApJ, 895, 80
Orio M. et al., 2023, ApJ, 955, 37
Orlando S., Drake J. J., Laming J. M., 2009, A&A, 493, 1049
Orlando S., Drake J. J., Miceli M., 2017, MNRAS, 464, 5003
Orlando S., Chomiuk L., Drake J. J., Miceli M., Bocchino F., Petruk O., 2025, A&A, 704, A144
Özdönmez A., Ege E., Güver T., Ak T., 2018, MNRAS, 476, 4162
Page K. L. et al., 2015, MNRAS, 454, 3108
Page K. L., Beardmore A. P., Osborne J. P., Orio M., Sokolovsky K. V., Darnley M. J., 2019, Astron. Telegram, 13084, 1
Page K. L. et al., 2020, MNRAS, 499, 4814
Pagnotta A., Schaefer B. E., 2014, ApJ, 788, 164
Polisensky E. et al., 2019, Astron. Telegram, 13185, 1
Rupen M. P., Mioduszewski A. J., Sokoloski J. L., 2008, ApJ, 688, 559
Sarbadhicary S. K., Badenes C., Chomiuk L., Caprioli D., Huizenga D., 2017, MNRAS, 464, 2326
Schaefer B. E., 2010, ApJS, 187, 275
Seaquist E. R., Taylor A. R., 1990, ApJ, 349, 313
Seaquist E. R., Krogulec M., Taylor A. R., 1993, ApJ, 410, 260
Shara M. M. et al., 2024, MNRAS, 529, 224
Shepherd M. C., 1997, in Hunt G., Payne H. eds, Astronomical Society of the Pacific Conference Series Vol. 125, Astronomical Data Analysis Software and Systems VI. California, Astronomical Society of the Pacific, San Francisco, p. 77
Skilling J., 1975, MNRAS, 172, 557
Sokoloski J. L., Luna G. J. M., Mukai K., Kenyon S. J., 2006, Nature, 442, 276
Sokolovsky K. V. et al., 2019, Astron. Telegram, 13050, 1
Starrfield S., Iliadis C., Hix W. R., 2016, PASP, 128, 051001
Steinberg E., Metzger B. D., 2018, MNRAS, 479, 687
Strader J. et al., 2019, Astron. Telegram, 13047, 1
Tang X., Chevalier R. A., 2017, MNRAS, 465, 3793
Vlasov A., Vurm I., Metzger B. D., 2016, MNRAS, 463, 394
Walder R., Folini D., Shore S. N., 2008, A&A, 484, L9
Walter F. M., Battisti A., Towers S. E., Bond H. E., Stringfellow G. S., 2012, PASP, 124, 1057
Weibel E. S., 1959, Phys. Rev. Lett., 2, 83
Weiler K. W., Panagia N., Montes M. J., Sramek R. A., 2002, ARA&A, 40, 387
Wenzel W., 1990, Inf. Bull. Var. Stars, 3517, 1
Weston J. H. S. et al., 2016, MNRAS, 457, 887
Wright A. E., Barlow M. J., 1975, MNRAS, 170, 41
Wrobel J., Walker R., 1999, Synthesis Imaging in Radio Astronomy II. Astronomical Society of the Pacific Conference Series. Astronomical Society of the Pacific, San Francisco, California, p. 171
Yaron O., Prialnik D., Shara M. M., Kovetz A., 2005, ApJ, 623, 398

APPENDIX A: A SYNCHROTRON HALO MODEL FOR THE LATE-TIME RADIO EMISSION

In this Appendix we outline a simple analytic model for the diffuse radio halo proposed in Section 5.4. The goal is not to provide a detailed numerical treatment, but rather to demonstrate that the observed radio luminosity, characteristic size, and spectral properties follow naturally from non-thermal particles escaping the γ-ray–producing shock into the red giant wind.

A1 Injection and Transport of Escaping Pairs

The late-time γ-ray luminosity is $L_\gamma \sim 10^{35.5}\,\mathrm{erg\,s^{-1}}$ (Fig. 7). If the γ-rays originate from hadronic interactions, a comparable power is injected into relativistic $e^\pm$ pairs through charged pion decay. We therefore parametrize the power injected into escaping pairs as

$$L_\pm = \xi_\pm L_\gamma, \tag{A1}$$

with $\xi_\pm \sim \mathcal{O}(1)$.

Pairs escape the dense acceleration region at a characteristic radius

$$r_0 \sim 10^{15}\,\mathrm{cm}, \tag{A2}$$

motivated by the VLBI size at $t \sim 50$ d (Table 1) and the timing of the second radio peak (Fig. 3). We take the injected pairs to have characteristic Lorentz factors $\gamma_{\pm,0} \sim 10^2$–10^4, in the range expected if the observed $E_\gamma \sim 1$–10 GeV emission arises from

Downloaded from academic.oup.com/mnras/article/552/4/stag1851/8842644 by Chalmers tekniska högskola (Chalmers University of Technology) user on 28 October 2026

neutral pion decay following inelastic pp collisions. The corresponding parent proton energies ($E_p \sim 10$–100 GeV) imply secondary $e^{\pm}$ from charged pion decay with energies $E_{\pm} \sim 0.1$–10 GeV, consistent with this range of Lorentz factors.

After escape, particles stream or diffuse outward with an effective radial speed $v_{\pm}$. To populate the halo out to $\sim 10^{16}$ cm within ~ 50 d requires $v_{\pm} \gtrsim 0.1c$. In steady state, conservation of particle flux gives a pair density profile

$$n_{\pm}(r) = \frac{\dot{N}_{\pm}}{4\pi r^2 v_{\pm}} = \frac{L_{\pm}}{4\pi r^2 v_{\pm} \gamma_{\pm,0} m_e c^2}. \tag{A3}$$

A2 Red giant wind high-density and magnetic-field

We assume a steady red giant wind with mass-loss rate $\dot{M}_w$ and velocity v_w, yielding a density profile

$$\rho(r) = \frac{\dot{M}_w}{4\pi v_w r^2}. \tag{A4}$$

We adopt $\dot{M}_w \simeq 2 \times 10^{-7}\, M_\odot\, \mathrm{yr}^{-1}$ and $v_w \simeq 10\, \mathrm{km\, s^{-1}}$, consistent with the X-ray constraints (Table 3).

We assume the wind carries a magnetic field that is approximately frozen into the flow. Beyond the Alfvén radius, a convenient scaling is

$$B(r) = B_* \left(\frac{R_*}{r}\right), \tag{A5}$$

where B_* is the red-giant surface field at radius R_*. For $B_* \sim 1$–10 G and $R_* \sim 1$ AU, this yields $B \sim 10^{-3}$–10^{-2} G at $r \sim 10^{15}$–10^{16} cm, comparable to the magnetic field strengths inferred in the shocked region (Table 2).

A3 Magnetic field amplification

The magnetic field calculated in the previous section assumes that the red giant wind has reached $r \sim 10^{16}$ cm since the previous (1990) nova eruption. Depending on the wind velocity, this may not be the case. However, we argue that $B \sim 10^{-3}$-10^{-2} is still a reasonable estimate. Not only can the post-shock region of the previous nova outburst contribute to the magnetic field at large radii, but escaping particles (ions and pairs) drive magnetic field amplification via streaming instabilities (e.g. E. S. Weibel 1959; J. Skilling 1975; A. R. Bell 2004). Assuming energy equipartition between the escaping pairs and the amplified field, we obtain,

$$\frac{B^2(r)}{8\pi} \sim u_{\pm}(r) \simeq \frac{L_{\pm}}{4\pi r^2 v_{\pm}}. \tag{A6}$$

Taking $v_{\pm} = 0.1c$, we find $B \sim 10^{-3}$ G for $L_{\pm} = L_{\gamma} = 10^{35}\, \mathrm{erg\, s^{-1}}$ and $r = 10^{16}$ cm.

A4 Slow cooling, characteristic frequency, and adiabatic losses

At the field strengths relevant here, synchrotron cooling is extremely slow compared to the transport/expansion time-scale. We therefore assume that pairs cool predominantly adiabatically as they propagate outward, so that

$$\gamma_{\pm}(r) \simeq \gamma_{\pm,0} \left(\frac{r_0}{r}\right). \tag{A7}$$

The characteristic synchrotron frequency at radius r is

$$\nu_{\mathrm{syn}}(r) \simeq 6\ \mathrm{GHz} \left(\frac{B_*}{1\,\mathrm{G}}\right)\left(\frac{R_*}{1\,\mathrm{au}}\right) \times \left(\frac{\gamma_{\pm,0}}{10^4}\right)^2 \left(\frac{r_0}{10^{16}\,\mathrm{cm}}\right)^2 \left(\frac{r}{10^{16}\,\mathrm{cm}}\right)^{-3}. \tag{A8}$$

so that GHz emission naturally arises at $r \sim 10^{16}$ cm for fiducial parameters.

The synchrotron cooling time is

$$t_{\mathrm{syn}}(r) \simeq 1.1 \times 10^4\ \mathrm{yr} \left(\frac{B_*}{1\,\mathrm{G}}\right)^{-2} \left(\frac{R_*}{1\,\mathrm{au}}\right)^{-2} \times \left(\frac{\gamma_{\pm,0}}{10^4}\right)^{-1} \left(\frac{r_0}{10^{16}\,\mathrm{cm}}\right)^{-1} \left(\frac{r}{10^{16}\,\mathrm{cm}}\right)^{3}. \tag{A9}$$

while the transport/adiabatic time-scale is $t_{\mathrm{ad}}(r) \sim r/v_{\pm}$. For the parameter space of interest, $t_{\mathrm{ad}} \ll t_{\mathrm{syn}}$ at all relevant radii, confirming that the pairs are in the slow-cooling regime.

A5 Radio luminosity and predicted flux density

A useful way to estimate the synchrotron output in the slow-cooling regime is to consider the energy contained in pairs within a logarithmic radial interval at radius r. The residence time in a shell of width $\mathrm{d}\ln r$ is $\sim r/v_{\pm}$, so the energy content is

$$\frac{\mathrm{d}E_{\pm}}{\mathrm{d}\ln r}(r) \simeq \left(\frac{r}{v_{\pm}}\right) \dot{N}_{\pm}\, \gamma_{\pm}(r)\, m_e c^2, \qquad \dot{N}_{\pm} = \frac{L_{\pm}}{\gamma_{\pm,0} m_e c^2}. \tag{A10}$$

Using $\gamma_{\pm}(r) = \gamma_{\pm,0}(r_0/r)$, the dependence on r and $\gamma_{\pm,0}$ cancels, giving

$$\frac{\mathrm{d}E_{\pm}}{\mathrm{d}\ln r} \simeq \frac{L_{\pm} r_0}{v_{\pm}} \simeq 1.4 \times 10^{40} \left(\frac{L_{\pm}}{10^{35.5}\,\mathrm{erg\, s^{-1}}}\right)\left(\frac{r_0}{10^{16}\,\mathrm{cm}}\right) \times \left(\frac{v_{\pm}}{0.1c}\right)^{-1}\ \mathrm{erg}. \tag{A11}$$

In the slow-cooling regime, the synchrotron power radiated from this interval is

$$\frac{\mathrm{d}L_{\mathrm{syn}}}{\mathrm{d}\ln r} \simeq \frac{1}{t_{\mathrm{syn}}(r)} \frac{\mathrm{d}E_{\pm}}{\mathrm{d}\ln r}. \tag{A12}$$

A convenient estimate of the spectral luminosity near the characteristic frequency emitted at radius r is then

$$L_{\nu}(r) \sim \frac{1}{\nu_{\mathrm{syn}}(r)} \frac{\mathrm{d}L_{\mathrm{syn}}}{\mathrm{d}\ln r} \sim \frac{1}{t_{\mathrm{syn}}(r)\, \nu_{\mathrm{syn}}(r)} \frac{\mathrm{d}E_{\pm}}{\mathrm{d}\ln r}. \tag{A13}$$

Substituting the expressions above and evaluating at the radius contributing to GHz emission (i.e. $r \sim 10^{16}$ cm for fiducial parameters) yields

$$L_{\nu} \simeq 4.7 \times 10^{19} \left(\frac{L_{\pm}}{10^{35.5}\,\mathrm{erg\, s^{-1}}}\right)\left(\frac{B_*}{1\,\mathrm{G}}\right)\left(\frac{R_*}{1\,\mathrm{au}}\right) \times \left(\frac{\gamma_{\pm,0}}{10^4}\right)^{-1} \left(\frac{r_0}{10^{16}\,\mathrm{cm}}\right)\left(\frac{v_{\pm}}{0.1c}\right)^{-1}\ \mathrm{erg\, s^{-1}\, Hz^{-1}}. \tag{A14}$$

The corresponding flux density is

$$F_{\nu} \simeq 0.88 \left(\frac{L_{\pm}}{10^{35.5}\,\mathrm{erg\, s^{-1}}}\right)\left(\frac{B_*}{1\,\mathrm{G}}\right)\left(\frac{R_*}{1\,\mathrm{au}}\right) \times \left(\frac{\gamma_{\pm,0}}{10^4}\right)^{-1} \left(\frac{r_0}{10^{16}\,\mathrm{cm}}\right)\left(\frac{v_{\pm}}{0.1c}\right)^{-1} \times \left(\frac{d}{6.8\,\mathrm{kpc}}\right)^{-2}\ \mathrm{mJy}. \tag{A15}$$

Downloaded from academic.oup.com/mnras/article/552/4/stag1851/8842644 by Chalmers tekniska högskola (Chalmers University of Technology) user on 28 October 2026

For $\xi_{\pm} \sim 1$ and $L_{\pm} \sim L_{\gamma} \sim 10^{35.5}\,\mathrm{erg\,s^{-1}}$, equation (A15) gives a fiducial flux density of order $F_{\nu} \sim 1\,\mathrm{mJy}$, below the ~ 3–$5\,\mathrm{mJy}$ diffuse component inferred from the EVN + e-MERLIN image of V3890 Sgr by a factor of a few. However, given the simplicity of the analytic estimate and the linear dependence of F_{ν} on uncertain quantities such as $B_{*}R_{*}$, r_0, and $v_{\pm}^{-1}$, this level of agreement is encouraging but should not be regarded as a detailed fit. For plausible parameters near the optimistic end of the allowed range, e.g. $B_{*}R_{*} \simeq 3\,\mathrm{G}\cdot\mathrm{au}$, $\gamma_{\pm,0} \sim$ few $\times\, 10^3$, $r_0 \simeq 10^{16}\,\mathrm{cm}$, and $v_{\pm} \simeq 0.1c$, equation (A15) gives F_{ν} in the range of the observed diffuse flux, given plausible parameters.

Finally, because $\nu_{\mathrm{syn}} \propto r^{-3}$ under the scalings adopted above, a broad range of radii contributes across a decade in observing frequency. This naturally produces a shallow, approximately power-law radio spectrum and a low-surface-brightness halo whose characteristic extent is set by particle transport.

Although non-thermal particles are produced throughout the eruption, the contribution of a given population to the observed GHz radio halo depends sensitively on the radius r_0 at which the particles escape the dense shock region. For particles injected at early times ($r_0 \ll 10^{15}$ cm), adiabatic losses reduce their Lorentz factors as $\gamma_{\pm}(r) \propto r_0/r$, so that by the time they reach radii $\sim 10^{16}$ cm their characteristic synchrotron frequencies lie well below the GHz band. In contrast, particles injected at later times, when the shock forms at $r_0 \sim 10^{15}$ cm, experience only modest adiabatic degradation and retain sufficient energy to emit efficiently at radio frequencies.

This effect is explicitly reflected in the scalings derived below: while the characteristic synchrotron frequency depends on both r_0 and r (equation A8), the normalization of the radio luminosity or flux scales linearly with r_0 (equation A15). As a result, late-time injection at larger radii naturally dominates the observable synchrotron halo, even if earlier shocks were more luminous in γ-rays.

This paper has been typeset from a TEX/LATEX file prepared by the author.

Downloaded from academic.oup.com/mnras/article/552/4/stag1851/8842644 by Chalmers tekniska högskola (Chalmers University of Technology) user on 28 October 2026

© The Author(s) 2026.
Published by Oxford University Press on behalf of Royal Astronomical Society. This is an Open Access article distributed under the terms of the Creative Commons Attribution License (https://creativecommons.org/licenses/by/4.0/), which permits unrestricted reuse, distribution, and reproduction in any medium, provided the original work is properly cited.